IEEE Transactions on Field Robotics (T-FR) paper, presented at ICRA 2026, Vienna, Austria. Cite as T-FR paper.

Aquaculture Robotics: Adaptive Path Planning Through Real-Time Estimation of the Shape of Flexible Net Pens

Herman B. Amundsen[1,2], Member, IEEE, Eirini Katsidoniotaki[3], Martin Føre[1], and Eleni Kelasidi[2], Member, IEEE

[1]Dept. Engineering Cybernetics, Norwegian University of Science and Technology, 7034 Trondheim, Norway
[2]Dept. Aquaculture Technology, SINTEF Ocean, 7010 Trondheim, Norway
[3]Dept. Mechanical Engineering, Massachusetts Instiue of Technology, Cambridge MA 02139, USA

Corresponding author: Herman B. Amundsen (email: herman.b.amundsen@protonmail.com).

This work was supported by the Research Council of Norway (RCN) under Grant 313737.

ABSTRACT

Aquaculture is a marine industry experiencing significant growth and an important seafood provider. Underwater vehicles such as remotely operated vehicles (ROVs) are commonly used for inspection and maintenance of the net pens where the fish are grown. These net pens are flexible structures whose position and shape change with ocean currents and waves. Any autonomous robotic operation in aquaculture is therefore challenging as the net pen position and shape cannot be predetermined and since it is imperative that the robot does not collide with and damage the net. This article addresses this issue by proposing a novel method to estimate the full shape of aquaculture net pens in real time using an underwater vehicle equipped with a forward-looking Doppler velocity log. The method introduces a new concept for how sparse measurement data on the net pen can be fused with numerical models of the full net pen that contrasts other models in literature by not requiring instrumentation on the net pen nor knowledge of ocean current conditions. The estimator output is then used in closed-loop vehicle control by planning and following paths relative to the estimated pen shape. The method is tested in simulations, which show an root mean square error (RMSE) of 0.5 m for estimate of the entire net pen structure and centimeter-level estimation error of the distance between the vehicle and net, and in full-scale trials in an industrial fish farm where an ROV autonomously navigated a net pen.

INDEX TERMS Aquaculture, Dynamic Environments, Marine Robots, Path Planning

I. INTRODUCTION

AQUACULTURE plays an important role in securing global food demands, and will likely play an even more crucial role going forward as the world population keeps growing. The intensive aquaculture industry has experienced rapid growth since its emergence in the 1950s, with the total production being multiplied by the hundreds over these decades. In 2022 aquaculture production surpassed capture fisheries for the first time, producing 51% of global seafood with a total production of 130.9 million tons worth 312.8 billion USD [1].

In sea-based aquaculture, the growth has been pioneered by the development of floating net pens, which are flexible structures that can deform with ocean waves and currents. As shown in Figure 1, a net pen typically consists of a net enclosure suspended from a circular plastic floating collar attached to a mooring system that is fastened to the seabed. The lower edge of the net enclosure is typically attached to point weights and/or a bottom weight ring (sinker tube) to extend the net pen and hence maintain a sufficient volume [2]. While dimensions vary, a typical fish farm can contain more than 10 net pens, each measuring 50 m in diameter and 30 m in depth, and containing up to 200,000 individual fish.

Fish farms have traditionally been placed in sheltered coastal waters since this reduces exposure to harsh weather and sealoads. However, due to a lack of available sites in sheltered areas and concerns related to parasite control and

©2026 IEEE

the sustainability of such sites, there is a trend of moving fish farms further offshore to more exposed sites [3], [4]. When faced with strong current velocities, net pens are prone to significant deformations that can reduce the net pen volume thus increasing fish density [2], [5], a parameter that is critical to animal welfare [6]. The response of net pens to current loads has therefore been the focus of many studies.

As production has been up-scaled, the aquaculture industry has struggled to maintain sustainability and faces several challenges, particularly related to fish welfare and environmental impacts [7]. Some of the most important of these challenges are related to the structural integrity and condition of the pens. For instance, fish escape incidents due to structural failure or net damages not only lead to production loss but also represent a grave environmental concern as escapees can harm wild fish populations through the spread of diseases and parasites, and interbreeding with wild fish [8], [9]. Biofouling on cage structures is another important challenge that may directly impair animal welfare since fouling can harbor parasites and reduce oxygen levels in the pen due to reduced water exchange [10]. To counter these and similar challenges, inspections and cleaning operations of net pens are frequent.

While divers are still used, the use of robotic platforms in inspection and maintenance operations in aquaculture has recently increased rapidly. ROVs in particular are commonly used for operations such as net inspections, biofouling removal, mooring line inspections, and fish monitoring [11]. To avoid tether entanglement risk with the complex mooring systems outside the net pens, such operations are usually performed inside the net pens. Pilots steer ROVs based on camera video and simple telemetry, and operations are usually conducted without automatic control beyond depth and heading hold. Although this practice has proven sufficient for many situations, it relies heavily on the abilities and experience of human pilots. This in turn means that ROV operations are limited by that pilots need to be in contact with the vehicle throughout missions, which may be challenging in harsher weather and more remote locations. Moreover, these activities often require planning in advance and depend on costly personnel and support vessels, making them one of the primary drivers behind the total costs of operations. In sum, this has induced an ongoing scientific effort to increase the autonomy level in ROV operations that aims to reduce costs, the risks of personnel injuries and the risks of human errors, while increasing the weather window for operations when moving further offshore [11].

In the underwater robotic domain, aquaculture represents an especially demanding environment with many unique challenges that are non-trivial to solve. Operations take place in the wave-zone [12] and in irregular ocean currents that are perturbed by the net and the biomass in the pen [13]–[15], which greatly affects control performance. Furthermore, sensor capabilities are often degraded, as hydroacoustic sensors suffer from scattering and multipath propagation effects due to the air-filled swim-bladders of the fish [16] and optical cameras are frequently affected by occlusions [17]. Finally, the environment in which the operations take place is highly dynamic and cluttered as it features flexible structures and living biomass. In this situation, safety is critical as collisions can harm the vehicle, the fish, and the net pen.

This paper proposes a novel method for autonomous inspection of net pens using unmanned underwater vehicles (UUVs). The method estimates the net pen shape by utilizing a dynamical model of a net pen that is corrected by measurements from a Doppler velocity log (DVL), and plans and updates vehicle paths relative to this estimated state. The following literature review will outline the foundation needed to develop this approach by including methods for

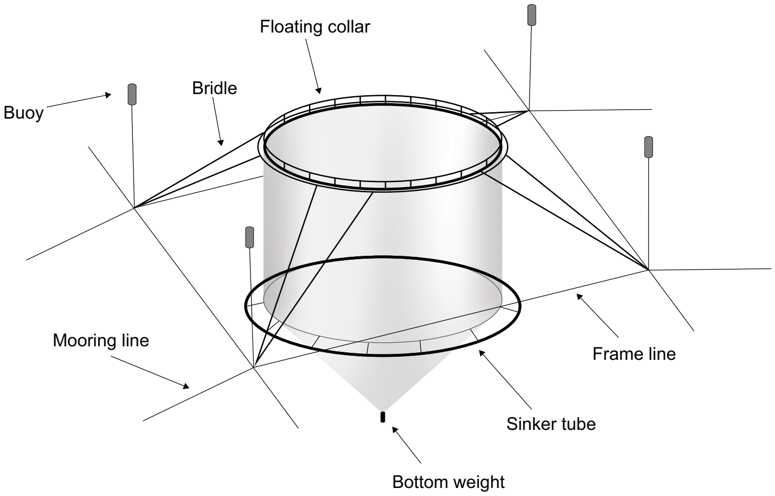

FIGURE 1. Illustration of a typical free-floating net pen. A cylindrical net enclosure with a conic bottom is suspended from a plastic floating collar. A sinker tube and bottom weight are attached to the net to maintain volume, while the floating collar is moored to the seabed with bridle chains, frame lines, and mooring lines.

modeling free-floating net pen dynamics and approaches to autonomous vehicle operations in aquaculture.

A. Related work

1) Modeling of net pens

Numerical modeling of net pens is a complex challenge. Due to the number of net twines comprising a net pen (typically in the order of tens of millions of individual twines) computational fluid dynamics (CFD) methods are computationally infeasible for real-time operations [2]. Furthermore, the net is affected by hydrodynamic interactions with the surrounding fluid and the internal potential energy caused by the elasticity of the net material, forming a complex and highly nonlinear problem.

Most approaches to modeling the hydrodynamic response of net pens can be split into two categories: Morison type and screen models. In Morison type models, the net is simplified to a finite number of interconnected trusses each representing a segment of the net. Each truss is given a length and diameter such that it has the same projected area as the physical net it represents, and Morison's equation [18] is then used to calculate the hydrodynamic force on each truss. The summed force on all trusses then represents the total force acting upon the net. See [5], [19], [20] for examples of studies using Morison-type models. Screen models are different in that the net is then divided into a number of screens, also referred to as net panels, and where the total hydrodynamic forces on a net pen are found as the sum of forces acting on all net panels. Løland [21] presented empirical formulas for lift and drag forces on net panels as a function of net solidity ratio (i.e., the ratio of the projected area of the net twines of a net panel to the total area of the net panel), the Reynolds number and inflow angle. Examples of studies that uses screen models include [2], [22]–[24].

The structural dynamics of the net is typically represented using a finite number of nodes connected with trusses that are subject to elongation through axial tension. In [23], the truss model of [25] was used, where the length of each truss is enforced by kinematic constraints. In [24], the kinematic truss constraint was given according to the feedback linearization method presented in [26], which was able to reduce the stiffness of the system while preserving the elasticity of the netting material.

Models representing the combined structural dynamics and hydrodynamics of net pens tend to be computationally complex and hence incur high computational loads, which can hinder their efficient use in real-time applications. A recent advancement that seeks to improve this is the use of machine learning methods to develop and train surrogate models that estimate the structural deformation of net pens [27], [28]. These models are then trained using data from more complex numerical simulation models run with various sealoads, to best mimic their outputs when exposed to such sealoads. Due to their much lower complexity, these models can then be used to quickly predict the deformation of pens given knowledge of environmental conditions.

Most methods for modeling net pens have been validated by numerical simulations or laboratory experiments. However, field validation of net pen models is more rarely done as it is difficult to reliably measure the full deformation of the pens. Previous studies aspiring to do this include using depth tags to measure the vertical displacements of strategic points in the net pen [28]–[30], fitting the net structure with acoustic sources and hydrophones [31] and attaching acoustic positioning transponders to the net [24]. A common denominator between these and similar field experiments is that they only measure a few points in the pen and then use numerical or surrogate modeling to extrapolate global pen deformation. In all cases, the models depend on knowing or estimating the relative velocity between the pen and water, which usually requires the use of current meters to measure current profiles, and costly installation of instrumentation to the net pen which may increase safety risks through the use of divers, and that may potentially lead to net damages [9].

2) Vehicle-autonomy in aquaculture

A fundamental challenge of most autonomous robotic systems is that of localization; without knowing the states of the robot, one cannot make informed decisions on future actions. In aquaculture, this is further complicated as the surroundings of the robot consisting of flexible structures and living fish are in a constant state of motion and most operational objectives are usually defined relative to the moving net pen [32]. It is therefore not enough to determine a georeferenced position of the robot, one must also determine the relative position between the robot and the net pen. This has prompted efforts to develop methods for estimating net-relative vehicle positions and attitudes.

An early study performed by [16] experimentally tested the performance of ultra-short baseline (USBL) acoustic positioning systems and DVLs in fish farms. Though the air-filled swimming bladders of fish can cause acoustic interference and multipathing, the USBL performance was found to be acceptable, indicating that acoustic positioning systems could be a viable part of underwater navigation systems in aquaculture. On the other hand, the DVL could not be used in a conventional setup as DVL bottom-lock will almost never be achieved in a pen since the fish and net bottom will be between the vehicle and the seabed and hence interfere with the hydroacoustic beams [16], [33]. However, [16] found that a DVL could be valuable when mounted forward-looking such that its beams are aimed at the net surface in front of the robot, yielding a *net-lock*. When reasonably close to the net ($\lessapprox 3$ meters), the field-of-view (FOV) will often be unobstructed, such that the DVL will yield accurate velocity measurements.

Another useful feature of a forward-looking DVL is that the measured length of the DVL beams can then be used to estimate the pose of the ROV relative to the net in front. This was the inspiration for the study in [34] which used the DVL measurements to approximate the geometry of a local region of the net in front of the robot, and further plan trajectories based on this approximation. While this allowed the robot to autonomously traverse the net at a constant safe distance, relieving operators of actively controlling the robot, the operator was still required to monitor the operation and change directions to gain full coverage during net inspections. This approach was further refined by [33] who replaced the DVL with a forward-looking multibeam sonar that yielded a more robust estimate of local net geometry as this sensor measured the positions of more points than the DVL. The study used the estimated inertial position of the robot to track inspection progress, and full visual coverage of target areas of the net was shown in experiments.

Sensory data required for underwater navigation can alternatively be obtained using cameras, which can generally be both cheaper and more widely available. In [35], visual tags were attached to the net such that computer vision could be used to compute the net-relative pose, which was then used for path planning. A different approach was used by [36] who equipped an ROV with two front-facing lasers, and used camera-laser triangulation to compute the net-relative pose. Moreover, several studies [17], [37], [38] have estimated the net pose through computer vision techniques by using features inherent to the net structure, such as meshes and ropes. In a more compound method, [39] fused computer vision techniques with DVL measurements to estimate both the local net-relative pose and the global position of the robot assuming a cylindrical net pen. Given these developments, that most robots are fitted with cameras and that the field of computer vision has developed at an impressive rate in the latest decade, camera-vision techniques represent an intriguing option to hydroacoustic sensors. However, the use of cameras in aquaculture is still challenging for a number of reasons. The visibility in pens may vary greatly since water often has high turbidity due to particles from, e.g., feed and feces, illumination can vary considerably and change rapidly and refraction varies with salinity. There are also practical challenges since occlusions are frequent, forces on the camera base from ocean waves and currents result in highly dynamic scene recordings, and there are few easily identifiable landmarks inside the net pens.

Common for all the aforementioned studies is that they use cameras or forward-looking sensors to estimate the position relative to the net in front of the robot. While this provides valuable information for planning safe trajectories as the distance to the net is estimated, it holds little validity outside a local region. An alternative can be to estimate both the state of the vehicle and the shape of the net pen, as this holds more information and thus provides more insight to obtain optimal plans and complete inspection routines. In [40], the method of [24] where a numerical model of a net pen was updated with measurements from acoustic short baseline (SBL) transponders attached to the net was used to plan net-relative paths. Similarly, [41] used forward-looking multibeam sonar measurements to estimate the net structure and planned vehicle paths based on the estimate, a solution they tested in simulations that assumed a rigid net structure. The main drawback of these methods is that they make assumptions regarding the structural properties and dynamics of the pen that might not accurately reflect reality, such that the estimated net pen shape may be incorrect. This can in the worst case compromise safety if the planned paths end up leading to collisions between the vehicle and the net.

Another important aspect of in-farm navigation is to take other parts of the net pen environment, such as instrumentation, ropes and cables, feeding systems, and biomass into account. These elements and their future positions are difficult to fully map and predict before executing an operation. Because of the safety-critical nature of aquaculture operations, it is therefore important to also incorporate more general obstacle avoidance into fully autonomous systems. Obstacle avoidance is a widely researched topic, but there are few examples where methods have been applied to aquaculture. In [42], the elastic band path planning method [43] was tested in an aquaculture setting, while [44] tested a motion planner with obstacle avoidance and active perception, representing to our knowledge the two first experimental tests of obstacle avoidance in aquaculture. However, none of these studies included the global net pen shape in the planning, thus indicating a research gap that should be targeted to realize safe autonomous operations in aquaculture settings.

B. Contributions

This paper proposes a new real-time method for concurrently estimating the shape of a net pen, and planning and executing autonomous collision-free missions relative to the net. The main contributions can be summarized as follows:

1) A novel net pen estimator is proposed. The method is based on a physical model of the net pen, which is affected by hydrodynamics, hydrostatics, and internal tension between the trusses in the structure. Further, the estimate is updated with DVL measurements by constraining the net to a point cloud made up by the acoustically measured positions. These constraints are enforced by adding proxy forces to the dynamical model. Compared to methods that extrapolate the net pen shape using measured data from a small number of sensors fixed to the net, the presented method is able to measure the net at many points as more measurement points are added as the vehicle moves, thus potentially enabling a higher fidelity estimate. Furthermore, as the method uses measurements from a sensor attached to the robot, the robot's local net-relative pose and distance can thus be accurately calculated, making the method less vulnerable to modeling errors compared to other net pen models when planning robot trajectories. By maintaining a complete estimate of the net pen, op-

timal trajectories and complete net inspections can be planned. Finally, unlike the net pen models presented in the literature review, the method does not depend on costly instrumentation of the net pen nor accurate knowledge of current velocities which in practice is often unavailable.

2) To navigate relative to the net, a net-relative waypoint following method is proposed. The method uses elastic bands path planning to reach waypoints that are defined relative to the net while maintaining a safe distance to the net and obstacles throughout the mission. Each waypoint is defined in cylindrical coordinates, which are mapped to Cartesian coordinates using the estimated net pen. Further, the path is updated in real-time with the net pen estimate, promoting safety and optimality even if the position and shape of the pen cannot be predetermined.

The performance of the methods are analyzed through simulations and full-scale field trials at an industrial fish farm. In the simulations, the net pen estimate is compared to a comprehensive net pen model, where the results show that the proposed estimator was able to capture the net pen shape with no knowledge of the current velocity. Moreover, the net-relative waypoint following method was demonstrated by the vehicle reaching all waypoints while staying at a safe distance to the net. In the field experiments, a 90-kg observer-class ROV was driven autonomously using the net pen estimation, with results supporting those from simulations.

To the authors' best knowledge, the method represents the first time an underwater vehicle is used to estimate the full shape of a net pen, and the results demonstrate how this can be used in a path planning context. The proposed method also represents a new tool for experimentally investigating the response of net pens to environmental loads. The commercial viability of the method is supported by that the method only depends on instrumentation already available to service companies providing ROV inspections in aquaculture. It is further noted that while the experiment in this article utilizes a DVL to measure the vehicle distance relative to the net, the method is general and can utilize any sensor capable of providing distance measurements.

The paper is organized as follows. First, Section II presents mathematical notations. Next, Section III describes the net pen estimation method, while Section IV proposes a net-relative path-planning method. Following this, Section V presents results from a simulation study, Section VI introduces the field experiment setup, and Section VII presents the results from the field experiments. Finally, Section VIII discusses the findings, Section IX presents lessons learned in this and previous field experiments in aquaculture, before Section X concludes the article.

II. Preliminaries

We let $\{n\}$ denote the north-east-down (NED) frame, which we assume is inertial, and let $\{b\}$ denote the body-fixed reference frame [45]. A matrix is denoted in boldface and upper-case, a vector is denoted in boldface and lower-case, and a scalar is denoted in regular roman font. The notation $\boldsymbol{z}^a$ denotes a vector $\boldsymbol{z}$, decomposed in the frame $\{a\}$, while $\boldsymbol{\Theta}_{ab}$ denotes the Euler angles from $\{b\}$ to $\{a\}$. The rotation matrix from the given frame $\{a\}$ to the given frame $\{b\}, \in SO(3)$, is denoted $\boldsymbol{R}_a^b$. The time-differentiation of a state x is denoted by $\dot{x}$.

III. Net pen estimation

A. Dynamic model

We base the net pen model on [24], with the addition of the correction from new measurements. To represent the net, we discretize the net pen to a finite set of nodes. In our implementation, we represented the pen with 10 depth layers, each with 32 nodes around the circumference. With the addition of the single bottom node, this adds up to 321 nodes in total. Further, each node is connected to a number of neighboring nodes such that the net pen is parametrically defined by a manifold. In general, a larger number of nodes would increase the fidelity of the estimate but at the cost of extra computational load.

Each node is associated with a three-dimensional position and velocity, which brings the total number of states in the model to 1926. We note that such a high number of states makes most state estimation techniques, such as traditional Kalman filters, infeasible for real-time purposes due to costly matrix inversion operations. Furthermore, the low number of measured states (a DVL typically measures four points) may lead to a loss of observability. This inspired us to tackle the challenge from a more physics-oriented approach instead.

We let the dynamics of node i be given by

$$\begin{aligned} m_i \ddot{\boldsymbol{x}}_i^n = \boldsymbol{f}_{ext}^n(\boldsymbol{x}_i^n, \dot{\boldsymbol{x}}_i^n, \boldsymbol{v}_c^n) + \sum_{k=1}^{N_i} \boldsymbol{t}^n(\boldsymbol{x}_i^n, \boldsymbol{x}_k^n, \dot{\boldsymbol{x}}_i^n, \dot{\boldsymbol{x}}_k^n) \\ + \sum_{m=1}^{M} \boldsymbol{c}^n(\boldsymbol{x}_i^n, \boldsymbol{x}_m^n)\,, \end{aligned} \tag{1}$$

where $\boldsymbol{x}_i^n \in \mathbb{R}^3$ is its position and $m_i > 0$ its inertia including added mass, $\boldsymbol{v}_c^n \in \mathbb{R}^3$ the current velocity which we for simplicity assume is similar over the entire structure, N_i the number of neighboring nodes and M the number of measured acoustic points. Further, $\boldsymbol{f}_{ext}^n(\cdot)$ is the external forces acting on the node, $\boldsymbol{t}^n(\cdot)$ the tension force from a neighboring node, while $\boldsymbol{c}^n(\cdot)$ is a proxy force between $\boldsymbol{x}_i^n$ and some measured point $\boldsymbol{x}_m^n$ which serves the purpose of updating the estimate with new measurements.

1) Internal tension

We calculate the internal tension between neighboring nodes, and between nodes and measured points, by using kinematic constraints. These constraints do not only serve the purpose of upholding coherent distances between neighboring nodes but also distributing external forces to the entire structure. When considering two neighboring nodes $\boldsymbol{x}_i^n$ and $\boldsymbol{x}_j^n$, the length of the truss connecting them is constrained by

$$C_{ij} = ||\boldsymbol{x}_i^n - \boldsymbol{x}_j^n|| - l_{ij} \ , \tag{2}$$

where l_{ij} is the natural truss length. Based on the Baumgarte stabilization technique and the feedback linearization formulation introduced in [26], we formulate the constraint force as

$$\boldsymbol{t}^n(\boldsymbol{x}_i^n, \boldsymbol{x}_j^n, \dot{\boldsymbol{x}}_i^n, \dot{\boldsymbol{x}}_j^n) = \\ \frac{\boldsymbol{x}_i^n - \boldsymbol{x}_j^n}{||\boldsymbol{x}_i^n - \boldsymbol{x}_j^n||} \left(k_{pl} C_{ij} + k_{dl} \left(\frac{(\dot{\boldsymbol{x}}_i^n - \dot{\boldsymbol{x}}_j^n)^T (\boldsymbol{x}_i^n - \boldsymbol{x}_j^n)}{||\boldsymbol{x}_i^n - \boldsymbol{x}_j^n||} \right) \right) \ , \tag{3}$$

where $k_{pl} > 0$ and $k_{dl} > 0$ are proportional and derivative gains. The proportional gain k_{pl} can also be recognized as the stiffness coefficient of the truss element. To set the axial dynamics of the truss element in accordance with the elastic modulus of the netting material, let

$$k_{pl} = \frac{E_{ij} A_{ij}}{||\boldsymbol{x}_i^n - \boldsymbol{x}_j^n||} \ , \tag{4}$$

where E_{ij} is the elastic modulus and A_{ij} is the cross-sectional area of the truss element. Finally, to maintain numerical stability, we require that the Courant number [46] remain upper bounded by one, which may require a reduction of the integrator step length or an adjustment of the natural frequency of the truss element, see [24] and [26].

2) External forces

We let the external forces be the sum of the hydrostatics and hydrodynamics, as well as forces from the floating collar and sinker tube and utilize the screen-model [23]. Figure 2 illustrates how the net is represented by nodes connected with trusses and surrounded by net panels. The hydrodynamic force on the net panels can be split into two components; a drag force in the same direction ($\boldsymbol{n}_d^n$) as the relative current velocity, and a lift force that acts normally ($\boldsymbol{n}_l^n$) to the relative current velocity. Using superposition, the total hydrodynamic force on a node is the sum of the hydrodynamic forces on the surrounding net panels, which are calculated using the drag term of Morison's equation [18]:

$$\boldsymbol{f}_{hd}^n(\dot{\boldsymbol{x}}_i^n, \boldsymbol{v}_c^n) = \sum_{j=1}^{\mathcal{P}_i} \frac{1}{2} \rho_w A_j ||\dot{\boldsymbol{x}}_i^n - \boldsymbol{v}_c^n||^2 (C_{D,j} \boldsymbol{n}_d^n + C_{L,j} \boldsymbol{n}_l^n) \tag{5}$$

where $\mathcal{P}_i$ is the set of surrounding net panels, ρ_w is the water density, and A_j is total area of net panel j. The drag and lift coefficients C_D and C_L are calculated from a Fourier series of the relative inflow angle, and are functions of Reynolds number and the solidity ratio. See [23] for a thorough description and study of these parameters.

The hydrostatic forces acting on node i are given by

$$\boldsymbol{f}_{hs,i}^n = (\rho_n - \rho_w) \boldsymbol{g}^n A_i d_w \ , \tag{6}$$

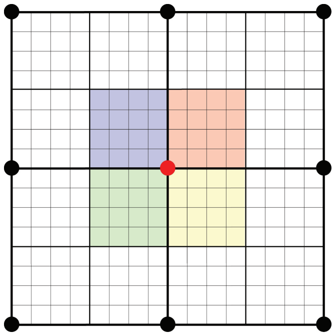

FIGURE 2. Decomposition of a net into an equivalent truss model [23]. The thick dots illustrates the numerical nodes of the model, connected with trusses (thick bars). The shaded areas represent the surrounding net panels that are used to calculate the hydrodynamic forces acting on the central node in red. Each net panel can cover multiple physical meshes of the net (thin lines).

where ρ_n is the netting density, $\boldsymbol{g}^n$ is the gravity acceleration vector, and d_w the twine diameter [18]. To simulate the impact of the bottom weight, the bottom node (with index 321) is also directly affected by the force from this weight ($\boldsymbol{f}_w^n$), such that

$$\boldsymbol{f}_{hs,321}^n = (\rho_n - \rho_w) \boldsymbol{g}^n A_{321} d_w + \boldsymbol{f}_w^n \ . \tag{7}$$

Unlike for the bottom weight, we use kinematic constraints to simulate external forces from the floating collar and sinker tube. This transfers the forces efficiently, while also ensuring that the net nodes connected to these components stay attached to them. Let $\mathcal{T}$ be the set of nodes connected to the floating collar and $\mathcal{B}$ be the set of nodes connected to the sinker tube. Using (3), the external forces from the floating collar and sinker tube are then given by

$$\boldsymbol{f}_t^n(\boldsymbol{x}_i^n, \boldsymbol{x}_t^n, \dot{\boldsymbol{x}}_i^n, \dot{\boldsymbol{x}}_t^n) = \begin{cases} \boldsymbol{t}^n(\boldsymbol{x}_i^n, \boldsymbol{x}_t^n, \dot{\boldsymbol{x}}_i^n, \dot{\boldsymbol{x}}_t^n), & i \in \mathcal{T} \\ 0, & \text{else} \end{cases} \tag{8}$$

and

$$\boldsymbol{f}_b^n(\boldsymbol{x}_i^n, \boldsymbol{x}_b^n, \dot{\boldsymbol{x}}_i^n, \dot{\boldsymbol{x}}_b^n) = \begin{cases} \boldsymbol{t}^n(\boldsymbol{x}_i^n, \boldsymbol{x}_b^n, \dot{\boldsymbol{x}}_i^n, \dot{\boldsymbol{x}}_b^n), & i \in \mathcal{B} \\ 0, & \text{else} \ , \end{cases} \tag{9}$$

respectively, where $\boldsymbol{x}_t^n$ and $\boldsymbol{x}_b^n$ are the position of the attached points in the floating collar and sinker tube. While both the floating collar and sinker tube in reality are elastic structures affected by external forces [47], we simplify by modeling both as rigid toruses for real-time purposes. We also model the sinker tube able to move in response to the current velocity and forces from connections to the net, while the floating collar is modeled as being statically placed at a fixed position.

The total external forces are then given by

$$\begin{aligned} \boldsymbol{f}_{ext}^n(\boldsymbol{x}_i^n, \dot{\boldsymbol{x}}_i^n, \boldsymbol{v}_c^n) = & \boldsymbol{f}_{hd}^n(\dot{\boldsymbol{x}}_i^n, \boldsymbol{v}_c^n) + \boldsymbol{f}_{hs,i}^n \\ & + \boldsymbol{f}_t^n(\boldsymbol{x}_i^n, \boldsymbol{x}_t^n, \dot{\boldsymbol{x}}_i^n, \dot{\boldsymbol{x}}_t^n) \\ & + \boldsymbol{f}_b^n(\boldsymbol{x}_i^n, \boldsymbol{x}_b^n, \dot{\boldsymbol{x}}_i^n, \dot{\boldsymbol{x}}_b^n) \ . \end{aligned} \tag{10}$$

3) Proxy forces from measurements

Consider a measured point $\boldsymbol{x}_m^n$. As this is a measurement of a point on the true net surface, we want to constrain the net to this point. However, as we have discretized the net structure, we may have a situation where the measured point is not reflected by the finite set of nodes, but rather by a point somewhere between the nodes. We therefore start by calculating the point on the estimated structure nearest to the measured point. First, let $\mathcal{P}_c$ be the set of nodes that defines the net panel closest to $\boldsymbol{x}_m^n$ and $\boldsymbol{n}_p^n$ be the normal vector of the net panel. The nearest point is then located at

$$\boldsymbol{x}_c^n = \boldsymbol{x}_m^n - \boldsymbol{n}_p^{n^T}(\boldsymbol{x}_m^n - \boldsymbol{x}_p^n)\boldsymbol{n}_p^n \ , \tag{11}$$

where $\boldsymbol{x}_p^n \in \mathcal{P}_c$.

To adjust the estimated net towards the measured point, we apply the following force to every node in the entire net structure:

$$\boldsymbol{c}^n(\boldsymbol{x}_i^n, \boldsymbol{x}_m^n) = e^{-\alpha||\boldsymbol{x}_i^n - \boldsymbol{x}_c^n||}\boldsymbol{t}^n(\boldsymbol{x}_c^n, \boldsymbol{x}_m^n, \boldsymbol{0}, \boldsymbol{0}) \ , \tag{12}$$

with $\alpha > 0$ being a tunable gain and $\boldsymbol{t}^n(\cdot)$ as given by (3). This force will move every node towards $\boldsymbol{x}_m^n$ along the direction from $\boldsymbol{x}_c^n$, but decay exponentially with the node distance to $\boldsymbol{x}_c^n$ such that the force will be stronger for nodes nearer to the measured point.

B. DVL measurements and filtering

As mentioned earlier, DVLs are typically mounted bottom-looking, and measure the velocity relative to the seabed by measuring the Doppler shift of the reflected hydroacoustic signals. The most common DVL configuration is the Janus configuration, which consists of four transducers pointing toward the fore, aft, port, and starboard of the vehicle [34].

For our case, the DVL is installed forward-looking. In accordance with Figure 3, the j-th DVL beam in sensor frame $\{d\}$ can be decomposed according to the vector

$$\boldsymbol{r}_j^d = \begin{bmatrix} x_j^d \\ y_j^d \\ z_j^d \end{bmatrix} = \left\|\boldsymbol{r}_j^d\right\| \begin{bmatrix} \cos(\gamma_j) \\ \sin(\gamma_j)\cos(\beta_j) \\ \sin(\gamma_j)\sin(\beta_j) \end{bmatrix} \ , \tag{13}$$

where $\left\|\boldsymbol{r}_j^d\right\|$ is measured and β_j, γ_j are the known rotations around the x and z axis of the DVL frame, respectively [34]. Let $\boldsymbol{r}_{b/\text{dvl}}^b \in \mathbb{R}^3$ be the lever arm from the vehicle center of origin to the DVL, and $\boldsymbol{p}_b^n \in \mathbb{R}^3$ be the position of the vehicle. Then, the j-th DVL beam is a measurement of the point

$$\boldsymbol{p}_{\text{dvl},j}^n = \boldsymbol{p}_b^n + \boldsymbol{R}_b^n\left(\boldsymbol{R}_d^b\boldsymbol{r}_j^d + \boldsymbol{r}_{b/\text{dvl}}^b\right) \ . \tag{14}$$

In reality, the measurement will be affected by noise, manifested through both the measured distance $\left\|\boldsymbol{r}_j^d\right\|$ and the estimated vehicle pose. The DVL measurements are especially prone to disturbances from the fish through scattering and multipath effects, which can introduce measurement outliers [34]. To improve robustness to measurement noise, we employ a Kalman filter with a four-dimensional state space, where the j-th state $\boldsymbol{x}_j$ is an estimate of $\boldsymbol{p}_{\text{dvl},j}^n$. If we let $\boldsymbol{y}_{\text{dvl},j}^n$ be a measurement of the true reflection point $\boldsymbol{p}_{\text{dvl},j}^n$, we can model the system as a linear system driven only by noise:

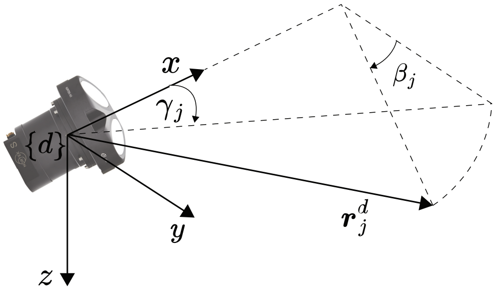

FIGURE 3. The vector components of the j-th DVL beam.

$$\dot{\boldsymbol{x}}_j^n = \boldsymbol{w}^n \tag{15}$$

$$\boldsymbol{y}_{\text{dvl},j}^n = \boldsymbol{x}_j^n + \boldsymbol{v}^n \ , \tag{16}$$

where $\boldsymbol{w}^n \in \mathbb{R}^3$ and $\boldsymbol{v}^n \in \mathbb{R}^3$ are process and measurement noise, respectively. We further include simple outlier rejection by rejecting measurements whose normalized innovation squares are above a threshold. The Kalman filter estimates are then fused with the dynamic net pen model through Eq. (12).

C. Improving from past measurements

While the method presented thus far is able to maintain a global estimate of the pen as well as an accurate local estimate by incorporating the DVL measurements, it will not be able to improve on the entire net pen estimate over time as the four measurement points move with the vehicle.

To improve the estimate as we receive more measurements, we maintain a bank with earlier Kalman-filtered measurements. Let $\mathcal{Y}_{t_o}^t$ be the set of filtered measurements from some previous time t_0 to the current time t. Further, partition $\mathcal{Y}_{t_o}^t$ into n subsets relative to specified time intervals $\Delta t > 0$. We then calculate the geometric median of each measurement state in each subset and add proxy forces per Eq. (12) using the geometric medians as $\boldsymbol{x}_m^n$. Reflecting on Eq. (1), the set M will thus consist of both current measurement states and the past geometric medians, such that the estimate will improve by considering older measurements. The maximum length of the measurement bank interval $t - t_0$ can be specified by the operator to forget older measurements as the net pen will move with changing environmental forces.

IV. Net-relative waypoint following

To utilize the net pen estimation to achieve vehicle autonomy, this section proposes a path planning method that adapts the path to reflect the current estimated shape.

In aquaculture robotics, many objectives are defined relative to the net structure, e.g., net inspections or net cleaning operations. From a pilot's point-of-view, it can often be beneficial to use cylindrical coordinates rather than Cartesian coordinates when maneuvering a net pen, as every point

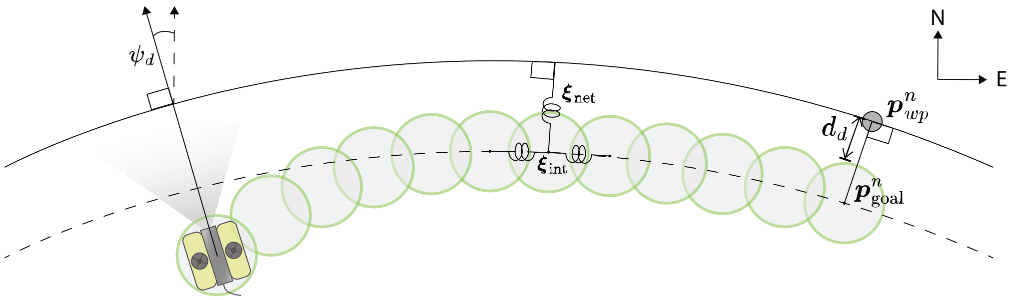

FIGURE 4. Net-relative elastic band waypoint following. The desired path is paved with bubbles from the current vehicle position to $\boldsymbol{p}^n_{\text{goal}}$, defined at a desired distance d_d from the waypoint $\boldsymbol{p}^n_{wp}$. At every timestep, each bubble is repositioned by considering internal tension ($\boldsymbol{\xi}_{\text{int}}$), attraction and repulsion from the net ($\boldsymbol{\xi}_{\text{net}}$), as well as repulsion from other obstacles or spatial constraints. The desired heading ψ_d is defined perpendicular to the net.

on the net will have a unique azimuth angle and depth which co-aligns with the pilot's compass and depth readings. Inspired by this and by previous work [48], the path planning framework is based on cylindrical coordinates and uses the estimated net pen to map these coordinates to Cartesian coordinates. To ensure safety and maintain the net within the FOV of the DVL, we let the operator specify a desired net distance for the vehicle and keep the desired heading perpendicular to the net.

We use the elastic band method [43] to plan collision-free paths to waypoints defined by the operator in cylindrical coordinates. In this method, the path is modeled as a mass-damper-spring system with dynamics mimicking those of a stretched elastic band where obstacles exert repulsive potential fields on the path and an internal potential field contracts the path to make it smoother, shorter, and more feasible. The path is initialized from a guess that may be in collision, usually a straight path to the goal position. This path is then iteratively optimized by letting the potential fields change its shape. The path is discretized and paved with a set of spheres, referred to as bubbles, with radii that vary with the free space and are lower bounded such that a bubble always encapsulates the entire volume of the vehicle.

Let $\boldsymbol{p}^c_{wp} = [\psi_{\text{net}}, z_{\text{net}}]^\top$ be the cylindrical position of a waypoint defined by the operator and let $d_d > 0$ be the desired distance we want to keep from the net. During the initialization phase, we first use the net pen estimate to map this coordinate to the inertial Cartesian reference frame, $\boldsymbol{p}^n_{wp} = [x, y, z]^\top$, and define the goal position by considering d_d:

$$\boldsymbol{p}^n_{\text{goal}} = \boldsymbol{p}^n_{wp} - (d_d + r_{\text{min}}) \frac{\boldsymbol{n}^n_{wp}}{\left\|\boldsymbol{n}^n_{wp}\right\|} , \tag{17}$$

where $r_{\text{min}} > 0$ is the lower bound of a bubble radius and $\boldsymbol{n}^n_{wp} \in \mathbb{R}^3$ the normal vector from the net at $\boldsymbol{p}^n_{wp}$. Finally, the path is initialized as a connected path from the vehicle position to $\boldsymbol{p}^n_{\text{goal}}$ (see Figure 4).

During each timestep, we first update the position of the first bubble with the current vehicle position and $\boldsymbol{p}^n_{\text{goal}}$ with the current net pen estimate. Next, the path is updated by considering potential fields from internal tension, the current net pen estimate, obstacles, and the sea surface.

Let the potential field simulating internal tension on bubble i be given by

$$\boldsymbol{\xi}_{\text{int}}(\boldsymbol{p}^n_{i-1}, \boldsymbol{p}^n_i, \boldsymbol{p}^n_{i+1}) = \frac{1}{2}\left(\left\|\boldsymbol{p}^n_{i+1} - \boldsymbol{p}^n_i\right\|\right)^2 \tag{18}$$

$$+ \frac{1}{2}\left(\left\|\boldsymbol{p}^n_i - \boldsymbol{p}^n_{i-1}\right\|\right)^2 , \tag{19}$$

where $\boldsymbol{p}^n_i$ is the position of bubble i. The formulation is inspired by Hooke's law and works to contract the path to avoid any "slackness" to the path [42].

Next, consider an obstacle that occupies the volume given by the set $\mathcal{O}$ and let $D(\boldsymbol{p}^n, \mathcal{O})$ represent the signed distance from some point $\boldsymbol{p}^n$ to $\mathcal{O}$. We then define a repulsive potential field acting on bubble i as

$$\boldsymbol{\xi}_{\text{obs}}(\boldsymbol{p}^n_i, \mathcal{O}) = e^{-D(\boldsymbol{p}^n_i, \mathcal{O}) - \epsilon} , \tag{20}$$

where $\epsilon \geq 0$ is a safety threshold. Similarly, to avoid generating a path over the sea surface, we include a repulsive potential field from the sea surface on the form

$$\boldsymbol{\xi}_{\text{surface}}(\boldsymbol{p}^n_i) = e^{-z_i \boldsymbol{e}^n_z} , \tag{21}$$

where z_i is the depth of $\boldsymbol{p}^n_i$ and $\boldsymbol{e}^n_z = [0, 0, 1]^\top$.

To maintain the desired distance to the net, two competing potential fields from the net are introduced, one being attractive and one repulsive. Consider a bubble position $\boldsymbol{p}^n_i$ and that the closest point on the net is given by $\boldsymbol{p}^n_{\text{net}}$. The combined potential field is given by

$$\boldsymbol{\xi}_{\text{net}}(\boldsymbol{p}^n_i, \boldsymbol{p}^n_{\text{net}}) = \frac{1}{2}\left\|\boldsymbol{p}^n_i - \boldsymbol{p}^n_{\text{net}}\right\| + e^{\left\|\boldsymbol{p}^n_{\text{net}} - \boldsymbol{p}^n_i\right\| - d_d - r_{\text{min}}} . \tag{22}$$

The former attractive term can be seen as an elastic where the tension is always constant, while the latter repulsive term decreases exponentially with the distance to the net. When close to the net, repulsion will dominate and push the path from the net, while the attractive term will dominate when far from the net. Further, the combined potential field is at an equilibrium when the path is at the desired distance from the net.

The total potential field is given by

$$\boldsymbol{\xi}(\boldsymbol{p}^n_{i-1}, \boldsymbol{p}^n_i, \boldsymbol{p}^n_{i+1}, \mathcal{O}, \boldsymbol{p}^n_{\text{net}}) = \boldsymbol{\xi}_{\text{int}}(\boldsymbol{p}^n_{i-1}, \boldsymbol{p}^n_i, \boldsymbol{p}^n_{i+1}) \tag{23}$$

$$+ \lambda_{\text{obs}} \boldsymbol{\xi}_{\text{obs}}(\boldsymbol{p}^n_i, \mathcal{O}) \tag{24}$$

$$+ \lambda_{\text{surface}} \boldsymbol{\xi}_{\text{surface}}(\boldsymbol{p}^n_i) \tag{25}$$

$$+ \lambda_{\text{net}} \boldsymbol{\xi}_{\text{net}}(\boldsymbol{p}^n_i, \boldsymbol{p}^n_{\text{net}}) , \tag{26}$$

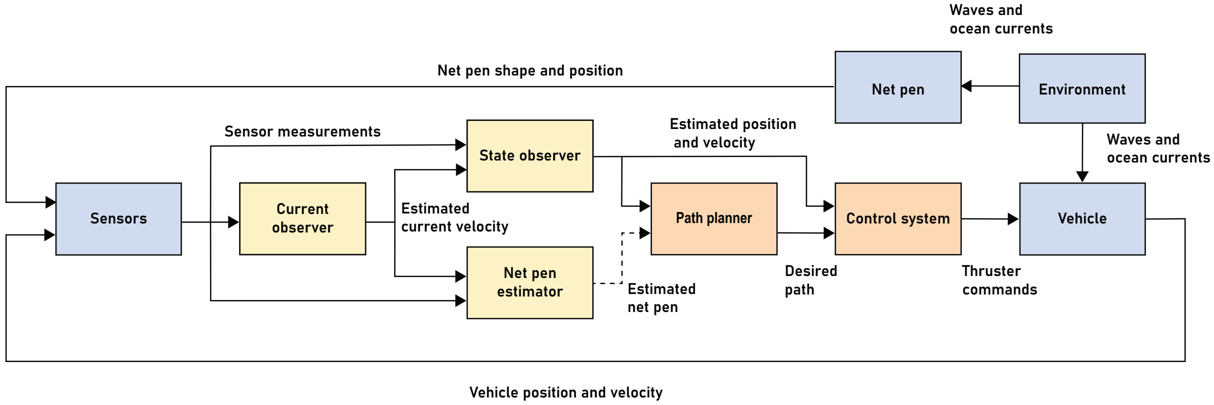

FIGURE 5. **Block model of the control system. During simulation-in-the-loop studies, the net pen, vehicle, environment, and sensor measurements (in blue) were simulated. During field experiments, these blocks were replaced by the actual physical systems they represented. During net-relative waypoint following, the estimated shape of the net pen was used by the path planner (dotted line), else the paths were planned independently of the net pen estimate.**

where $\lambda_{\text{obs}} > 0, \lambda_{\text{surface}} > 0, \lambda_{\text{net}} > 0$ are gains, while the update rule is given by

$$\boldsymbol{p}_i^n[k+1] = \arg\min_{\boldsymbol{p}_i^n} \boldsymbol{\xi}_i[k] + (\boldsymbol{p}_i^n - \boldsymbol{p}_i^n[k])\nabla\boldsymbol{\xi}_i[k] \,, \qquad (27)$$

where $k \in \mathbb{N}$ refers to the iteration number of the gradient descent, ∇ is the functional gradient operator, and $\boldsymbol{\xi}_i[k] = \boldsymbol{\xi}(\boldsymbol{p}_{i-1}^n, \boldsymbol{p}_i^n[k], \boldsymbol{p}_{i+1}^n, \mathcal{O}, \boldsymbol{p}_{\text{net}}^n[k])$. The final step of the algorithm is to update path resolution and the bubble radii according to the new path configuration and the available free-space.

V. Simulation study

Prior to field deployment, we conducted an extensive set of simulations that helped us understand the challenges and limitations of the method. The simulation studies also gave us a chance to compare the state from the net pen estimation to a surrogate net pen model that served as the ground truth in simulations. We implemented the simulation as similar as possible to the setup planned in the field experiment, and, in particular, kept the navigation and control system identical to how it would be during field deployment. This section will first present the simulation setup and then results from four simulation studies.

A. Simulation setup

The simulation studies were performed in FhSim, a numerical modeling and simulation framework with a focus on marine systems hosted by SINTEF Ocean [49]. In the control system (Figure 5), a model-based ocean current observer estimated the current velocity based on the sensor measurements. The current velocity estimate and the sensor measurements were given as inputs to a state observer and the net pen estimator described in Section III. During net-relative waypoint following, the path planner described in Section IV calculated the desired path by utilizing the estimated net pen shape. Finally, the control system used the planned path and the state estimates to calculate the thruster commands, which in turn together with simulated environmental forces were used to drive the dynamic vehicle model.

TABLE 1. **Simulation case studies**

Sim. no.	Path planning	Current estimation
1	Net following [34]	Current observer
2	Net following [34]	No estimation
3	Net-relative waypoint following	Current observer
4	Net-relative waypoint following	Current observer

We performed a set of four simulation studies as summarized in Table 1. The first two simulations were used to analyze the performance of the net pen observer specifically, first with and then without using the current observer to examine its robustness when subjected to poor current velocity estimations. These simulations used the net following method from [34] to plan trajectories that guided the ROV to traverse the net at a constant distance. Since the third simulation targeted the net-relative waypoint following method specifically, it was set up with the path planning method proposed in Section IV and used the pen observer with the current observer. The final simulation was intended to test the net pen observer under stronger ocean currents and for a longer duration and used net-relative path planning to inspect the net pen in a lawn-mower pattern.

1) Environmental model

The net pen and vehicle models were subjected to ocean currents and wave forces simulated by the environmental model. Waves were generated in accordance with the JONSWAP wave spectrum with a significant wave height of $H_s = 1.5$ m, a mean wave period of $T_1 = 7$ s, and a mean wave direction of $\psi_{\text{wave}} = 180°$. According to the definition of sea state codes, this is characterized as a moderate sea state [45], with a dominant wave direction from the south. In the first three case studies, the current velocity was chosen constant and irrotational and set to $\boldsymbol{v}_c^n = [0.4, 0, 0]^\top$ m/s, while it was given as $\boldsymbol{v}_c^n = [0.8, 0, 0]^\top$ m/s in the final simulation.

2) Net pen model

To serve as the ground truth in simulations, we used the model of [27]. This machine-learned surrogate model is based on Gaussian process regression and establishes a relationship between incoming ocean waves and current parameters and net pen deformation. As it is more computationally efficient compared to numerical methods, it offers rapid predictions. The model is trained on a dataset generated by the numerical model in [24] which included 1,000 simulations representing a wide range of ocean wave and current conditions, with corresponding estimates of net pen deformation for each case. The net pen had a radius of $r = 25$ m, a cylindrical shape down to a depth of 15 m and then a conic shape extending to a depth of 28 m. Further, the net was set up with a solidity ratio of $S_n = 0.236$ (this number is usually given in the net pen data sheet), and an elastic modulus of $E = 10$ GPa, which is a dimension typical in aquaculture [24].

3) Net pen observer

The net pen observer from Section III was set up with structural properties equal to those used in the net pen model. We let the tunable gain of (12) $\alpha = 0.1$, which was found to give a good response, as a larger value will diminish the proxy forces such that the net pen estimate do not reflect measurements, while a smaller value leads to larger proxy forces that might cause instability. Furthermore, we chose to partition $\mathcal{Y}_{t_0}^t$ into subsets relative to time intervals of 30 s as this was found to yield a good "memory" of past measurements without causing conflicts that might arise if the geometric medians are very close to one another. No prior assumptions were made about the current velocity, i.e., the net cage was initially subjected to a current velocity of $\hat{\boldsymbol{v}}_c^n(t_0) = [0, 0, 0]^\top$.

4) Vehicle model

The simulated vehicle was a 90 kg ROV with six thrusters, yielding control in surge, sway, heave and yaw. As we assume a constant and irrotational current, the following maneuvering model is applied [45]:

$$\begin{aligned} \dot{\boldsymbol{\eta}} &= \boldsymbol{J}(\boldsymbol{\eta}) \left(\boldsymbol{\nu}_r + \begin{bmatrix} \boldsymbol{v}_c^n \\ \mathbf{0}_{3\times 1} \end{bmatrix} \right) \\ \boldsymbol{M}\dot{\boldsymbol{\nu}}_r + \boldsymbol{C}(\boldsymbol{\nu}_r)\boldsymbol{\nu}_r &+ \boldsymbol{D}(\boldsymbol{\nu}_r)\boldsymbol{\nu}_r + \boldsymbol{g}(\boldsymbol{\eta}) = \boldsymbol{\tau}_c + \boldsymbol{\tau}_{\text{wave}} \,, \end{aligned} \tag{28}$$

where $\boldsymbol{\eta} = [\boldsymbol{p}_b^{n\top}, \boldsymbol{\Theta}_{nb}^\top]^\top$ is a generalized position vector consisting of the inertial position $\boldsymbol{p}_b^n$ of the vehicle and its orientation $\boldsymbol{\Theta}_{nb}$, $\boldsymbol{J}(\boldsymbol{\eta}) \in \mathbb{R}^{6\times 6}$ is the transformation vector from the body-fixed frame to the inertial frame [45], $\boldsymbol{\nu}_r = \boldsymbol{\nu} - \boldsymbol{\nu}_c^b = [u_r, v_r, w_r, p, q, r]^T$ is the relative velocity between the body-fixed generalized vehicle velocity $\boldsymbol{\nu} \in \mathbb{R}^6$ and the generalized current velocity $\boldsymbol{\nu}_c = \boldsymbol{J}^{-1}(\boldsymbol{\eta})[\boldsymbol{v}_c^{n\top}, 0_{3\times 1}^\top]^\top$, $\boldsymbol{\tau}_c \in \mathbb{R}^6$ are the control forces, and $\boldsymbol{\tau}_{\text{wave}} \in \mathbb{R}^6$ are the wave forces.

Furthermore,

$$\begin{aligned} \boldsymbol{M} =& \boldsymbol{M}_{RB} + \boldsymbol{M}_A \\ =& \text{diag}(90, 90, 90, 10, 15, 13) \\ &+ \text{diag}(54, 72, 360, 11, 43.5, 5.2) \end{aligned} \tag{29}$$

is the combined rigid body and added mass matrix,

$$\begin{aligned} \boldsymbol{D}(\boldsymbol{\nu}_r) &= \text{diag}(250, 200, 175, 20, 20, 15) \\ &+ \begin{bmatrix} 350|u_r| & 0 & 0 & 0 & 0 & 0 \\ 0 & 350|v_r| & 0 & 0 & 0 & 0 \\ 0 & 0 & 400|w_r| & 0 & 0 & 0 \\ 0 & 0 & 0 & 100|p| & 0 & 0 \\ 0 & 0 & 0 & 0 & 100|q| & 0 \\ 0 & 0 & 0 & 0 & 0 & 75|r| \end{bmatrix} \end{aligned} \tag{30}$$

is the damping matrix, $\boldsymbol{C}(\boldsymbol{\nu}_r) \in \mathbb{R}^{6\times 6}$ is the Coriolis-centripetal matrix which can be parameterized from $\boldsymbol{M}$, and $\boldsymbol{g}(\boldsymbol{\eta}) \in \mathbb{R}^6$ represent the restoring forces. The thrusters were modelled with saturation and rate limitations.

5) Sensor models

The vehicle was fitted with simulated sensors, including an USBL acoustic positioning system, a forward-looking DVL, an attitude-heading reference system (AHRS), a pressure sensor for depth measurements, and a gyroscope for measurement of angular rates. All sensor systems were simulated with output rates, measurement noise, and measurement outliers in accordance with the performance of the actual sensors. In particular, the DVL only provided measurements when the net pen was in the direction and range of the DVL beams. Further, to simulate the effect of the fish on the DVL beam distance measurements, each measurement had a standard deviation of $\sigma_{\text{dvl}} = 0.15$ m, a dropout rate of 15% on top of the measurement frequency of 8 Hz, and an outlier percentage of 5%, where outliers were uniformly distributed between the sensor blanking distance and twice the distance to the net.

6) Ocean current observer

The ocean current observer proposed in [50] was used to estimate the current velocity. The observer can be recognized as a constant gain nonlinear model-based Luenberger observer and updates the current estimate by fusing the vehicle model with the latest measurements of the generalized velocity, angular velocity, and orientation, respectively, from the DVL, gyro and AHRS. To include model uncertainty in the simulation, we let the vehicle model parameters by increased by 5% relative to (28).

7) State observer

We employed a 4 degree-of-freedom (DOF) model-based extended Kalman filter as a state observer for the vehicle.

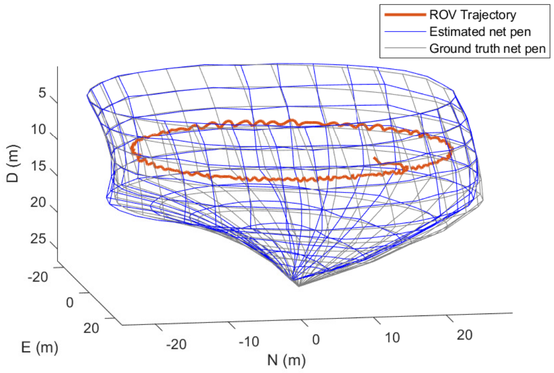

FIGURE 6. **Simulation of net pen estimation with local net following and estimated current velocity from ocean current observer.**

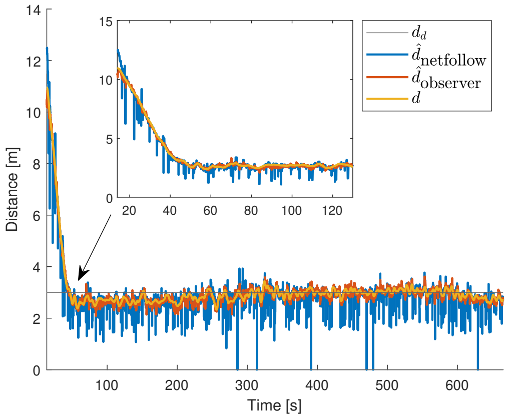

FIGURE 7. **Desired (d_d), actual (d) and estimated ($\hat{d}_{\text{observer}}$) distance to the net compared against the method of [34] ($\hat{d}_{\text{netfollow}}$) in simulation with local net following and ocean current observer.**

We utilized the 4DOF counterpart to (28) as the model, calculated the relative velocity using the estimate from the ocean current observer, and considered measurement updates from the USBL, pressure sensor, AHRS, DVL and gyro. A bias model was included to compensate for slowly-varying forces and model uncertainties [42], [45]. As for the current observer, we simulated parameter uncertainty by multiplying the parameters in $\boldsymbol{M}$ and $\boldsymbol{D}(\boldsymbol{\nu}_r)$ by 1.05.

8) Control system

Given the thruster setup of the vehicle, we are only controlling the surge, sway, heave, and yaw of the vehicle. We used a line-of-sight (LOS) guidance law [51] to calculate the desired velocity $\boldsymbol{v}_d^b(t) = [u_d(t), v_d(t), w_d(t)]^\top$ of the vehicle, and let the desired heading $\psi_d(t)$ be perpendicular to the estimated net pen. To control the vehicle states, the generalized super-twisting algorithm [52], [53] which is a higher-order sliding mode controller with good robustness to time and state-dependent uncertainties was utilized. Finally, control allocation was used to find the control signal of each thruster [45].

B. Net pen estimate with local net following

In the first simulation study, the net following method [34] was set to traverse the net at a constant distance of $d_d = 3$ m and a depth of $z_d = 8$ m. Using the DVL to estimate the local geometry of the net in front of the vehicle, the method generates a desired velocity that guides the vehicle to traverse the net in the starboard direction. While the first simulation used the current velocity estimated by the current observer, the net pen observer was set up with a constant current velocity of $\hat{\boldsymbol{v}}_c^n = [0, 0, 0]^\top$ in the second simulation to render the method oblivious to the ocean current estimate.

The simulation results demonstrated that the net pen observer obtained good estimates of the entire net pen shape and position (Figure 6) with the average root mean square error (RMSE) across all final node position states being $\overline{\text{RMSE}}(\tilde{\boldsymbol{x}}_{\text{end}}) = 0.55$ m. The reason for this deviation is that the vehicle only inspected the net pen at a single depth, and hence the net pen estimator had little information to correct its estimate at other depths. Further, the average standard deviation across all nodes were $\overline{\boldsymbol{\sigma}}_x = [0.53, 0.37, 0.32]^\top$ m. Figure 8 demonstrates how the estimation error evolves with local measurements. Here, the RMSE of four nodes are compared to their distance to the ROV from which it can be seen that their error reduces as the ROV passes their neighborhood and is kept low from there on out. The fidelity of the estimate is well within the requirements for path planning, especially as it was able to accurately estimate the local net-relative distance (Figure 7). This indicates that the method is more robust to DVL measurement outliers than the method in [34] and that it can accurately estimate the shape of inspected areas close to the vehicle.

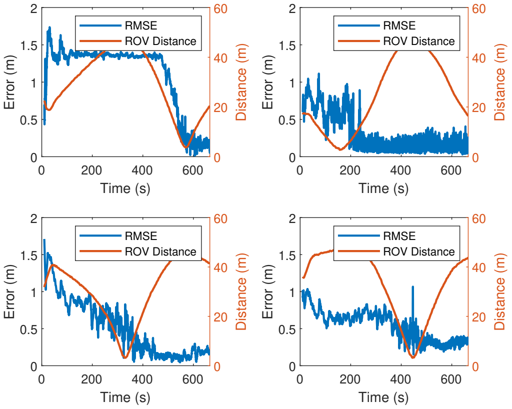

FIGURE 8. **RMSE of the estimatated position of four nodes at the north, east, south, and west side of the net pen compared to their distance to the ROV during simulation with local net following and ocean current observer.**

Interestingly, the performance of the net pen estimator did not change considerably in the second simulation, as seen in

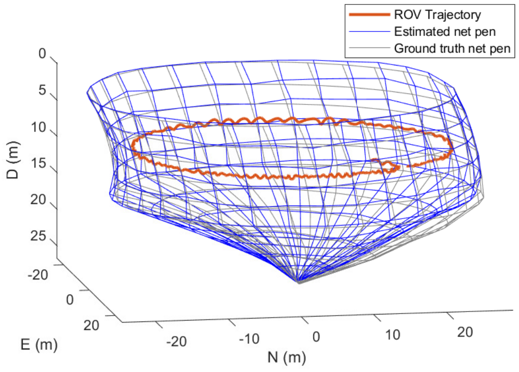

FIGURE 9. Simulation of net pen estimation with local net following and no ocean current estimation.

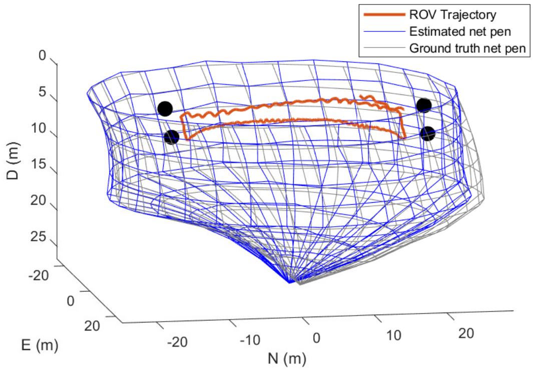

FIGURE 10. Simulation of net-relative waypoint following. The waypoints are indicated with black spheres.

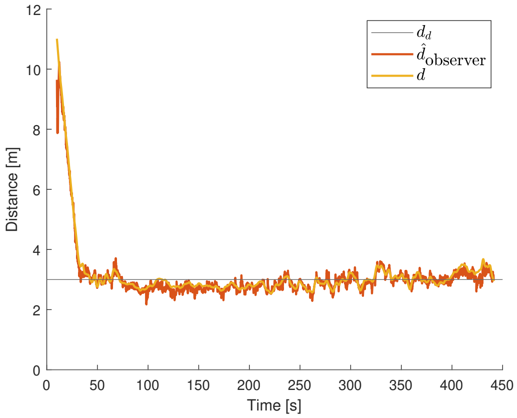

FIGURE 11. Desired (d_d), actual (d) and estimated ($\hat{d}_{\text{observer}}$) distance to the net during simulation of net-relative waypoint following.

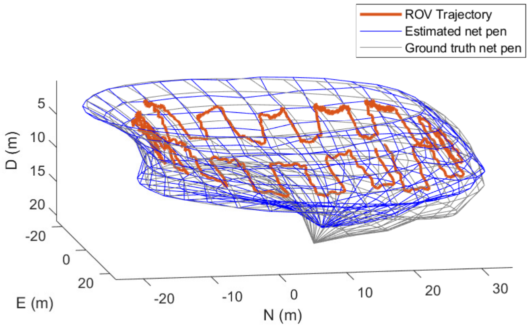

FIGURE 12. Simulation with net-relative waypoint following under effect of strong ocean currents.

Figure 9. This is mainly because the hydrodynamic forces are dominated by the proxy forces from the DVL measurements as given by (12). In this case, the average RMSE of the final node positions were $\overline{\text{RMSE}}(\tilde{x}_{\text{end}}) = 0.51$ m, a slight improvement over the first simulation. In sum, these results suggest that the net pen observer can estimate the net pen shape and position with high accuracy, even without knowledge of the ocean current velocity.

C. Net-relative waypoint following

Four waypoints were considered in the net-relative waypoint following simulation: $\boldsymbol{p}^c_{wp,1} = [-\pi/6, 6]^\top, \boldsymbol{p}^c_{wp,2} = [-\pi/6, 10]^\top, \boldsymbol{p}^c_{wp,3} = [-2\pi/3, 10]^\top, \boldsymbol{p}^c_{wp,4} = [-2\pi/3, 6]^\top$ and the vehicle was commanded to reach them sequentially before returning to $\boldsymbol{p}^c_{wp,1}$. These form a square pattern on the net wall, and the vehicle was controlled to keep a distance $d_d = 3$ m from the net. We let $r_{\text{min}} = 0.65$ m, $\lambda_{\text{surface}} = 1/2$, $\lambda_{\text{net}} = 3/2$, and $\lambda_{\text{obs}} = 0$ as no external objects were present. In general, these gains can be seen as weights which determines how the total potential field (23) is assembled from $\xi_{\text{int}}, \xi_{\text{obs}}, \xi_{\text{surface}}, \xi_{\text{net}}$. The gains were determined by trial and error and by prioritizing the potential from the net over the internal and the surface potentials. A waypoint was considered reached when the vehicle entered the bubble of the elastic band placed relative to the waypoint, which in practice happened when the waypoint was in the vehicle's FOV at a safe distance. The vehicle successfully reached all waypoints (Figure 10), and was able to keep a safe distance to the net throughout the simulation (Figure 11). Furthermore, the accuracy of the net pen estimation supported the results from the other simulations since the highest accuracy was along the side of the pen traversed by the ROV, i.e., where the estimation was corrected by measurements.

D. Net inspection with strong ocean currents

The goal of the final simulation was to test the net pen observer when the net pen was influenced by strong ocean currents and during long-term missions. In these simulations, the ocean currents were twice as strong ($||\boldsymbol{v}^n_c|| = 0.8$ m/s) and the waypoints were defined in a lawn-mower pattern such that the ROV would perform a more comprehensive inspection compared to the former simulation case studies.

The desired distance to the net was set to $d_d = 1.5$ m and the total mission duration was 48 min.

When influenced by such strong currents, the net pen will by severely deformed, as seen in Figure 12. While upper cylindrical section of the estimated net pen correlated nicely to the ground truth, it can be seen that bottom conic section deviated from the ground truth, which was supported by that the error was larger compared to the other simulations, $\overline{\text{RMSE}}(\tilde{x}_{\text{end}}) = 0.93$ m. Still, the accuracy of the net pen estimate was sufficient to be used by the path planner to successfully navigate the ROV along the net pen.

VI. Experimental setup

This section presents the setup of field trials conducted at SINTEF ACE Singsholmen, an industrial-scale salmon farming site outside the island of Hitra, Norway [54]. This fish farm consists of several free-floating net pens and is part of the SINTEF ACE laboratory, a cluster of fish farming sites dedicated to the research and development of aquaculture technology. Our experimental plan was based on progressively increasing the complexity of the trials: 1) perform preliminary tests of modular components of the control system, 2) test autonomy in an empty net cage without fish, and 3) test autonomy in a fully stocked cage. However, due to stormy weather, we were prevented from performing the final autonomy tests with fish, which is thus left as future work. We therefore present results of a preliminary test from the first day with the presence of fish, and two extensive experiments from the second day without the presence of fish. The hydroacoustic sensors were thus affected by the fish only in the preliminary test, and the results from this test were thus important to analyze the method's efficacy in the presence of fish, while the other experiments were used to test the control system in autonomous operation, the novel net estimator, and net-relative path following method. All structural components and dimensions of the empty pen were similar to those of the pen holding the fish.

The net pen was of the same dimension as the net pen model from Section V, with a radius of $r = 25$ m, and a cylindrical depth of 15 m, and a bottom cone with a depth of 13 m. The net solidity was specified as $S_n = 0.236$, however, in reality, this will vary with the degree of biofouling on the net [55].

The vehicle used in the experiments was an Argus Mini ROV (Figure 13), a 90 kg observation class ROV developed by Argus Remote Systems AS whose main properties and configuration match those of the simulated vehicle used in the simulation studies. Its dimensions are $L \times W \times H = 0.9$ m $\times$ 0.65 m $\times$ 0.5 m, and it has four horizontal and two vertical thrusters (Argus 800W, capable of forces up to 117.5 N) arranged to actuate the vehicle in surge, sway, heave, and yaw. Further, the ROV was fitted with an HD camera, a forward-looking DVL (Nortek DVL 1000), and a transponder (Sonardyne Nano) for acoustic positioning with a USBL system (Sonardyne MicroRanger 2). We did not have access

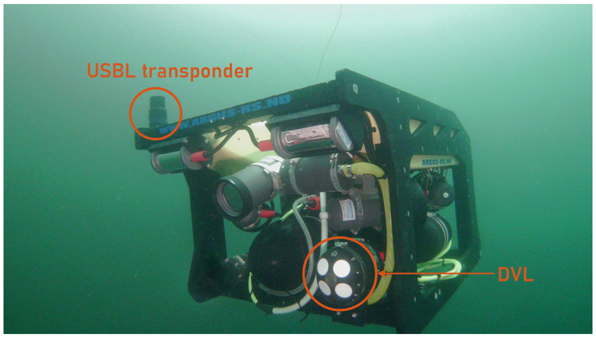

FIGURE 13. **Argus Mini ROV equipped with a USBL transponder and a forward-looking DVL deployed at SINTEF ACE Singsholmen fish farm.**

FIGURE 14. **M/S Torra docked at SINTEF ACE Singsholmen fish farm.**

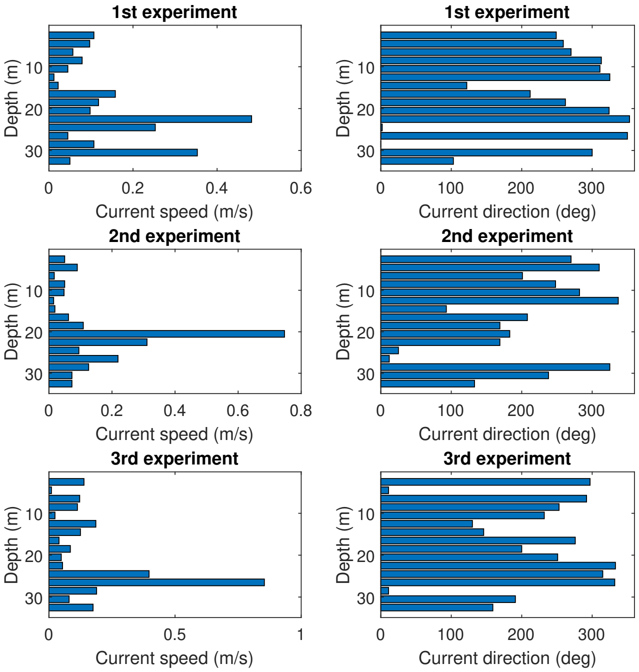

FIGURE 15. **Measured ocean current speed and direction at the time of the first, second and third experiments.**

to high-rate inertial measurement unit (IMU) measurements, but instead received estimated orientation, yaw rate, and depth from its onboard AHRS and depth estimator at 10 Hz.

The ROV was teleoperated using a topside control computer onboard a 14 m support vessel (depicted in Figure 14), and the origin of the inertial reference frame was defined at the position of the ROV operator. The topside control computer could switch between manual control with a joystick and autonomous control, and relayed control signals to each thruster. During autonomous control, the control system was implemented identically as in the simulation experiments (Figure 5, Section V). The net pen estimation and net-relative path planner operated at 100 Hz.

The fish farm featured an acoustic Doppler current profiler (Nortek Aquadopp 600 kHz) that provided measurements of the speed and direction of the ocean current every 10 minutes. The measurements were not used by the control system but were used for data analysis, looking at both speed and heading at different depths (Figure 15). Measured current speeds and directions varied with depth with speeds being generally slow (< 0.1 m/s) near the surface and faster (> 0.5 m/s) at specific layers deeper in the pen.

VII. Experimental results

Here, we present the results from the field experiments. Similar to the simulation study, the system was tested with and without net-relative waypoint following. The first experiment was a preliminary trial where the ROV was piloted in manual control along the net while the net pen observer estimated the pen's shape. In the second experiment, the net following method of [34] was used to traverse the net while maintaining a constant distance to the net, running the proposed net pen observer in the background, but not using its outputs as inputs to the control system. These case studies enabled an isolated look at the performance of the pen observer, with the first experiment also providing data on how the sensors performed in the presence of biomass. Finally, in the third experiment, the net-relative waypoint following method presented in Section IV was tested using the estimated net pen shape in closed-loop control.

A. Experiment 1: Preliminary trial

In the first experiment, the ROV was maneuvered for about 14 m along the net for two minutes. Figure 16 shows the estimated trajectory of the ROV and the final state of the net pen estimation. As the ROV traversed only a small segment of the net pen, the net pen observer did not receive enough info to estimate the full deformation of the net pen, and, as the measured points did not deviate considerably from the nominal shape of the net pen, the estimate was close to what would be expected when the net pen is unaffected by currents and waves.

A more interesting observation can be made from the results in Figure 17. When compared with the net distance

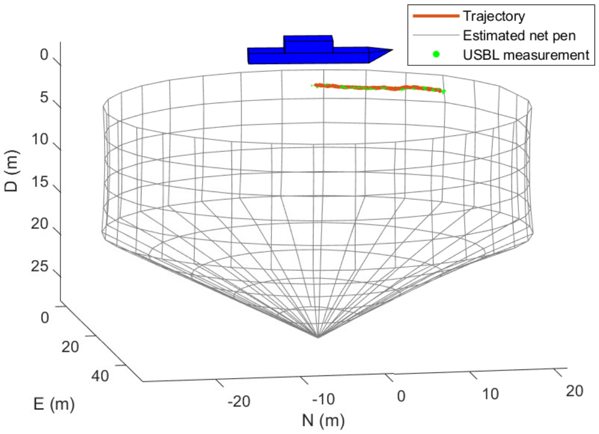

FIGURE 16. **Net pen estimation with manual control in the presence of fish. The position of the support vessel is indicated in blue.**

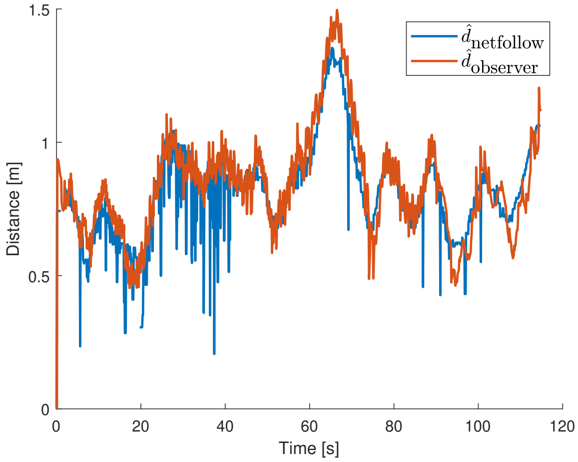

FIGURE 17. **Estimated distance to the net ($\hat{d}_{\text{observer}}$) compared with the method of [34]($\hat{d}_{\text{netfollow}}$) during manual control.**

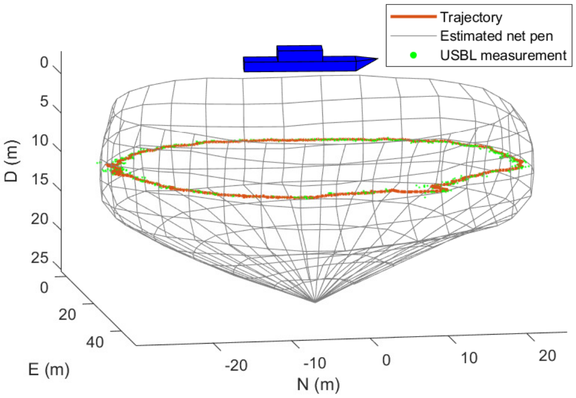

FIGURE 18. **Net pen estimation with net following. The position of the support vessel is indicated in blue.**

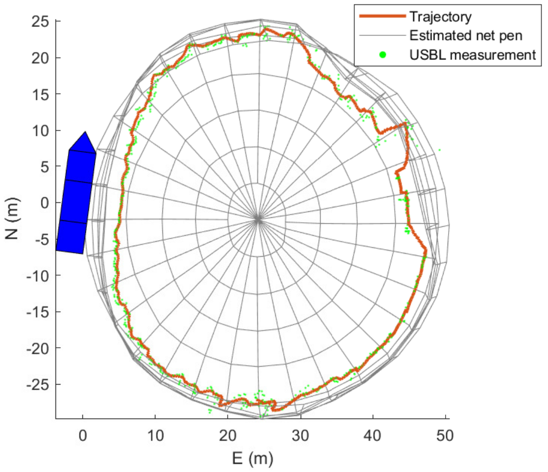

FIGURE 19. **Net pen estimation with net following seen from above. The position of the support vessel is indicated in blue.**

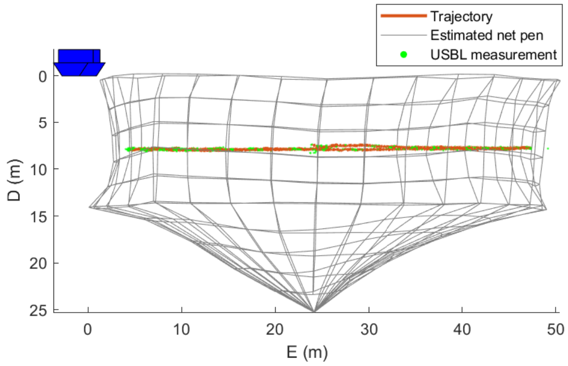

FIGURE 20. **Net pen estimation with net following seen from the south. The position of the support vessel is indicated in blue.**

estimation from [34], it is clear that both methods estimate similar distances with the proposed method having less noise in the estimates. This corresponds well with simulation results and is probably because the method used by [34] was susceptible to DVL noise due to fish intercepting the hydroacoustic beams whereas these outliers were handled by the Kalman filter in the present method.

B. Experiment 2: Net pen observer with local net following

The setpoints for the net following method of [34] was a desired distance to the net of $d_d = 2$ m and a desired depth of $z_d = 8$ m, and we let the vehicle traverse the inner perimeter of the net pen in a full circle.

The final state of the estimated net pen can be seen in Figures 18-20. This estimate suggest that the net pen was contracted along the east axis and prolonged along the north axis. This fits well with measured ocean current velocity (Figure 15), which showed that the fastest current speeds were in the south direction suggesting that there should be a hydrodynamic drag on the net in this direction that should deform the pen accordingly.

The estimated trajectory was also affected by noise due to outliers in the USBL measurements, in particular around 210 s (or ca. “two o’clock” in Figure 19) where outliers caused a jump in the estimated position. While it may look like there was a collision at this position, the plotted net pen represents the final estimated state at the end of the experiment (i.e., around 650 s) and thus does not reflect the estimated shape at 210 s which show that no collision took place (Figure 21). This is also supported by that the estimated distance, both according to the proposed net pen observer and the method of [34], stayed close to the desired distance and at a safe distance throughout the experiment (Figure 22). The two different methods were affected differently by measurement noise during these trials. Based on the obtained results and the analysis, we are convinced that the primary cause for this difference is that the approach used by [34] is more susceptible to noise in the DVL measurements, while the proposed net pen observer is likely more susceptible to noise in the position estimate, as these noise processes affect (14) differently. The average computation time for a time step by the net pen observer was 0.51 ms, while the worst case computation time was 2.58 ms, well within real-time requirements.

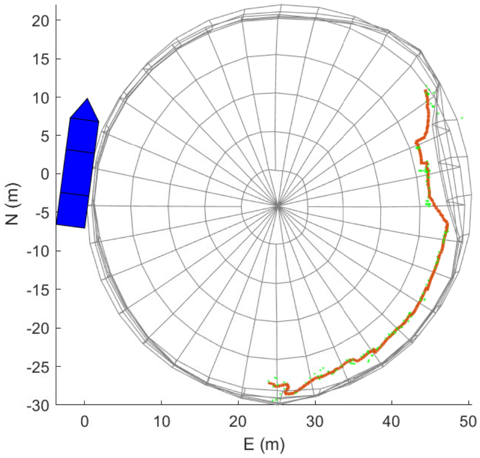

FIGURE 21. **Net pen estimation with net following seen from above at 210 s. The position of the support vessel is indicated in blue.**

C. Experiment 3: Net-relative waypoint following

The waypoints considered in the experiment were defined as $\boldsymbol{p}^c_{wp,1} = [-\pi/3, 3]^\top$, $\boldsymbol{p}^c_{wp,2} = [-2\pi/3, 3]^\top$, $\boldsymbol{p}^c_{wp,3} = [-2\pi/3, 9]^\top$, $\boldsymbol{p}^c_{wp,4} = [-\pi/3, 9]^\top$, and, as in the simulation studies, the vehicle was commanded to reach them sequentially before returning to the first waypoint. The desired distance to the net was set at $d_d = 1.5$ m.

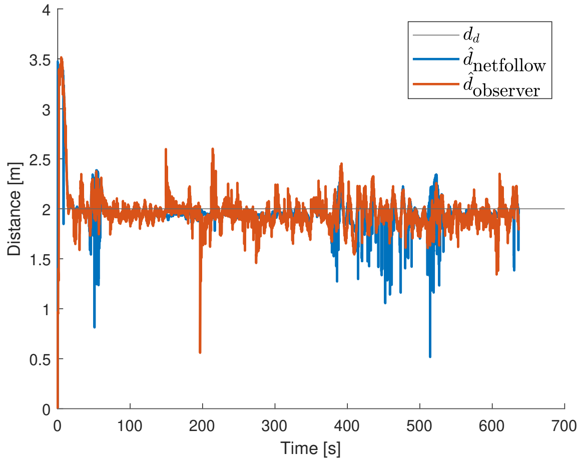

FIGURE 22. **Desired (d_d) and estimated ($\hat{d}_{\text{observer}}$) distance to the net compared with the method of [34]($\hat{d}_{\text{netfollow}}$) when using net pen estimation with net following.**

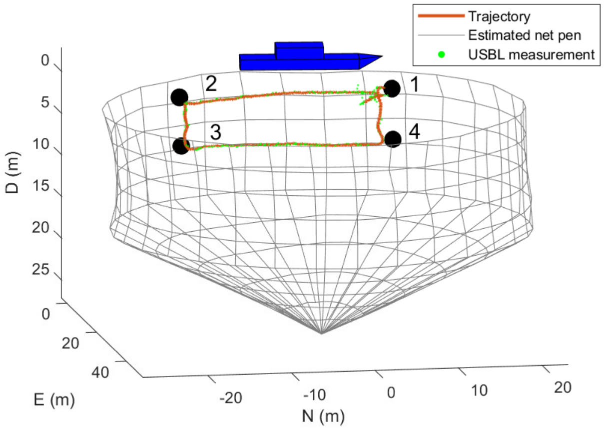

FIGURE 23. **Net pen estimation with net-relative waypoint following. The position of the support vessel is indicated in blue, while waypoints are indicated with black spheres.**

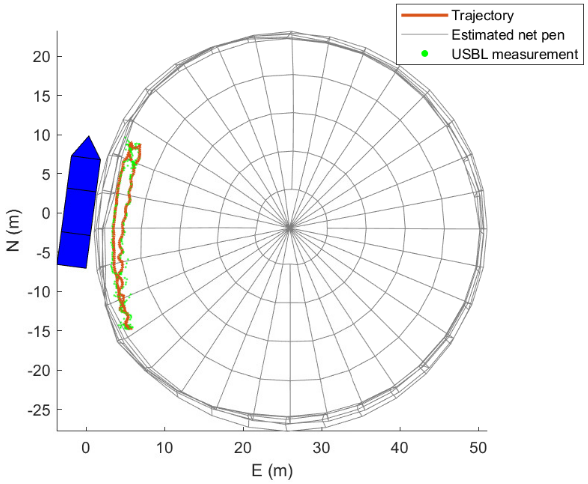

FIGURE 24. **Net pen estimation with net-relative waypoint following seen from above. The position of the support vessel is indicated in blue.**

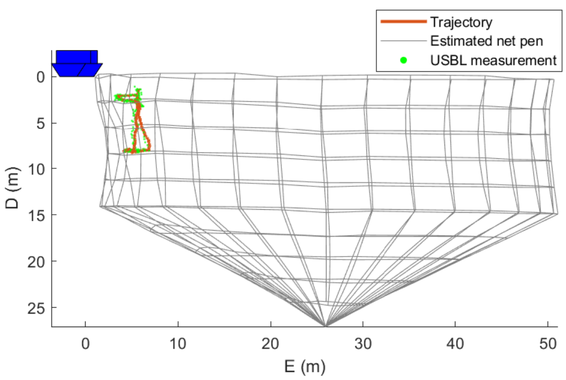

FIGURE 25. **Net pen estimation with net-relative waypoint following seen from the south. The position of the support vessel is indicated in blue.**

The method managed to guide the ROV to all waypoints while staying at a safe distance from the net (Figure 23 and Figure 26). Between 150 s and 200 s, an oscillation is visible in the net distance. The cause of this oscillation was that the most recent filtered DVL measurements ($\boldsymbol{x}_m^n$ in (12)) where in close proximity to calculated geometric medians of past measurements. However, the position of those geometric medians were not in agreement with the most recent DVL measurements, which caused an oscillation in the net pen estimate as the proxy forces competed.

The net pen shape estimated in the closed-loop experiment (Figures 23-25) was different from the one obtained in the net following experiments (Figure 18-20). This is probably mainly because the current profile changed between the second and the third experiment (Figure 15) which led to an actual difference in pen shape. Another factor likely to contribute to this is that the ROV only traversed the net along its western side in the closed-loop trial, and, as such, did not have sufficient measurements to accurately estimate the shape along the northern, southern, and eastern sides of the pen.

The average computation time for the net pen observer was 0.37 ms, while the worst-case computation time was 1.33 ms. In addition, the average and worst-case replanning time for the path planner was 0.14 ms and 1.16 ms, respectively.

VIII. Discussion

In this section, we discuss our findings and future prospects of the proposed method. Autonomous navigation within or near flexible three-dimensional structures whose changes in position and shape cannot be predetermined, such as net pens, remains a considerable challenge in underwater robotics. The proposed method represents a new way to address this challenge by estimating net pen geometry using a numerical model updated with measurements from the vehicle's sensors. This approach paves the way for advance-

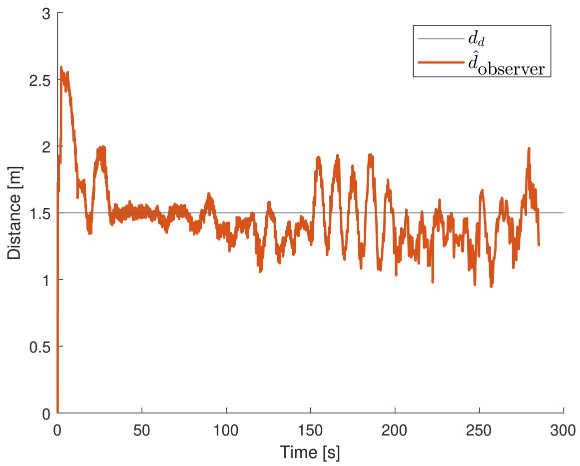

FIGURE 26. **Desired (d_d) and estimated ($\hat{d}_{\text{observer}}$) distance to the net when using pen estimation with net-relative waypoint following.**

ments in aquaculture robotics, as it enables safe net-relative navigation while maintaining an awareness of the vehicle's position relative to the entire net pen.

The presented method relies upon measuring points of the net pen and is not tied to the use of any specific sensor to achieve this. In the field experiments, a DVL was used to measure points in the body-fixed frame, which were then transformed to the inertial frame using the vehicle pose estimated with aid from the DVL and USBL. It might be possible to achieve a good position estimate without the use of USBL as the DVL provides velocity measurements or by, e.g., using alternative methods such as visual odometry [56]. Similarly, the point cloud does not need to be measured by a DVL, but can also be measured by, e.g., sonars or computer vision methods [39].

When estimating the entire pen shape, there exists an injective mapping from points defined on the net pen manifold in cylindrical coordinates to Cartesian coordinates, which enables net-relative navigation. Our experiments demonstrated the possibility of reaching waypoints defined relative to the net, which can be practical if the aim is inspection or intervention tasks targeting specific points on the net (e.g., for repairing holes). This also opens another potential venue in enabling coverage path planning [57], which means the planning of complete paths that pass the sensor over the entire net pen manifold to ensure full coverage since such planners require an accurate map of the manifold. Another application of the new estimation method is that it can be useful during manual operations by helping the pilot maintain an overview of the ROV position inside the net pen and the progress of net inspections, which may be challenging as there are few visual landmarks. This was found very useful during the experiments, underlining the method's utility also in commercial inspection missions.

While the estimator worked well during the trials, future improvements of the net model could improve its accuracy and precision. During the implementation of the net pen model, model fidelity had to be prioritized lower than real-time capabilities. Since this will lead to a less realistic estimate of the net structure, a future aim is to improve the fidelity of the net pen model. This will entail modeling the dynamics of the sinker tube and, especially, the floating collar using more realistic representations. These are both flexible structures that deform in response to external forces, and the floating collar in particular is also strongly affected by wave forces, especially in high seas. The present implementation assumed that the floating collar was a static torus, which did not fit well with the experimental data (see, e.g., Figure 19).

We also found that when geometric medians and DVL measurements are in close proximity to one another, their respective proxy forces can compete against each other which may cause oscillations to the net pen estimate. A potential fix to this problem is to disregard older geometric medians that are in close proximity to measurements or more recent geometric medians. Another aspect that was observed during the trials was that the net pen estimator relied upon a good choice of integration parameters to avoid instabilities. This can lead to challenges, as using parameters that differ slightly from those that are most appropriate would result in impaired performance. One way of solving this can be to improve the node dynamic model, e.g., with a more sophisticated inertia, which might improve stability properties and relax the requirement for specific integration parameters.

In the trials, all the trajectories tested related to the upper cylindrical part of the net pen, while there were no trajectories seeking to follow the net in the bottom cone of the pen. The main reason for this is that the DVL was mounted forward-looking and, as such, performs best when the orientation of the target net wall is close to normal to the axis between the vehicle and the net wall. While this is the case in the cylindrical part of the pen, the net wall will be at an oblique angle when in the bottom cone. This can in turn render the DVL unable to get a net-lock when navigating along the bottom cone. One way to improve this and thereby facilitate net-relative navigation and hence inspection in the bottom cone is to enable the adjustment of the tilt angle of the sensor.

Although the methods were successful in navigation in a net pen environment, another future aim is to validate closed-loop control using the net pen estimator and net-relative path planner in a net pen with fish. This would test the methods' abilities to cope with or suppressing the adverse effects of the fish on the acoustic sensors, which is a crucial step in enabling the use of these methods in commercial situations.

IX. Lessons learned

Over several years, we have conducted several field experiments in aquaculture robotics, a challenging marine domain, and had our fair share of successes and failures. In this section, we will discuss some of the lessons we have learned.

Underwater engineering remains challenging due to the harsh and unforgiving nature of the environment. Specifically, vehicle control is challenging due to hydrodynamics, communication capabilities are limited due to the high signal attenuation in water, and seawater corrosion causes deterioration of equipment. Aquaculture operations are also exposed to weather conditions, which can increase health, safety, and environment (HSE) risks [58] and reduce the weather window where operational conditions are considered acceptable, while robots in aquaculture operate in highly dynamic environments consisting of flexible structures and living fish.

We've had persistent challenges with acoustic position systems such as USBL in that the accuracy and the dropout rate of the measurements have varied between experiments; from experiments where the performance has been well within the error tolerances of the system, to experiments where it has been challenging to get converging measurements. These problems are likely due to multipath propagation and scattering effects. We have thus learned that USBL system settings should be adapted to the different environmental conditions encountered at different sites and that it is often best to start with a low transmit power, and then tune until an acceptable signal-to-noise ratio (SNR) is achieved. However, since frequent and long dropout periods can still occur, it is important to use state estimators with acceptable performance during dead-reckoning.

Our experience with DVL has shown that this sensor can measure velocity and distance relative to the net accurately. By setting a high transmit power, net-lock will be achieved when its FOV is unobstructed. Bottom-lock can generally only be obtained outside of a net cage, and net-lock can only be obtained when reasonably close to the net (typically closer than 5 m). We have also seen that the outliers caused by DVL measurements being intercepted by fish schools are generally easy to detect and reject, and that dropout periods are usually short.

Past experiments have also highlighted the challenges of using cameras for navigation purposes in aquaculture. Light attenuation can vary considerably in water and is affected by turbidity, which can be high in aquaculture due to e.g., feed spills, feces and matter released by biofouling. One effect of this is that colored light with low energy (e.g., red) is quickly absorbed and as a result, green and blue typically dominate the underwater color spectrum. Another challenge is that the net has a repeated structure that can make finding easily distinguishable landmarks hard. Furthermore, it is not uncommon for camera images to be occluded due to the fish passing between the camera and the net. As such, it is not straightforward to adapt computer vision techniques that have been successful in other domains to be used for underwater navigation inside aquaculture net pens. In the future, it is possible that optical sensors attached to robots hold great potential in aquaculture, not only for navigation purposes but also for applications such as 3D photogrammetry mapping of the net pens which can be valuable for improving reporting from ROV net inspections. However, this will require more refined methods for pre- and post-processing the results from these instruments to cope with the different challenges mentioned above.

Tether management is a difficult task, particularly when navigating the outside of the net pen. Fish farms have complex mooring systems, and power lines and feeding lines also connect the pens with the feeding barge. While inspections outside of the net pen are possible to conduct, tether management will then require a constant focus, and it is usually best to split inspection tasks into segments where there are fewer cables and ropes that can cause entanglement. If the autonomy level can be increased to a point where the vehicle can safely operate without human surveillance, the tether can be removed, which would represent a milestone in aquaculture robotics that would mitigate the risk of entanglement completely. However, due to the high safety requirements in aquaculture, this requires a higher level of autonomy than the current standards, as well as rigorous experimental validation.

While the risk of entanglement is lower when navigating inside net pen, such applications require keeping a greater responsibility towards the fish population. Vehicle operations could be harmful to the fish not only through direct collisions but also by the mere presence of the vehicle potentially inducing a higher stress level which may in turn have negative health consequences [59]–[61]. Fast vehicle maneuvers can cause flight responses in the fish, which may be related to an increase in stress levels. Further, we have also experienced that when operating in a specific part of a net cage over time, it appears that the fish population will try to avoid this area. Further research is required to understand the interaction between robotic operations and the fish population better. Such knowledge may in turn be used as a foundation for developing new vehicle designs and operational guidelines that are more gentle towards the fish, while still being able to solve autonomous missions.

Finally, vehicles should be designed in a way that reduces the risk of damaging the net or harming the fish. In particular, sharp edges to the vehicle or tools should be avoided as this can cause tear to the net, and thrusters should be covered with lattices to avoid fish getting caught by the propellers.

X. Conclusion

This paper presented a method to estimate in real-time the shape of an aquaculture net pen using a remotely operated vehicle equipped with a forward-looking Doppler velocity log (DVL). By leveraging a numerical model of a net pen and introducing proxy forces that constrained the net to the acoustic points measured by the DVL, the net pen observer was able to update the estimate with measurements. This contrasts with state-of-the-art methods that either only estimate the vehicle position relative to a local region of the net, or use models to extrapolate the complete pen shape from measurements from sensors fixed to the net, an approach that requires expensive instrumentation and is susceptible to modeling errors.

Further, a path planning method that can guide the vehicle to waypoints defined relative to the net pen was proposed. By utilizing the estimated net pen, which updates in real-time, the path was updated to ensure that it stays collision-free. Furthermore, the path was kept at a constant distance and the field of view of the robot perpendicular to the net, enabling inspection tasks.

The method was tested in field experiments at an industrial salmon farm situated on the coast of Norway. The results showed that the method was able to estimate the net pen shape and the vehicle's distance to the net, even without prior knowledge of ocean currents. Furthermore, the vehicle was successful in reaching the waypoints while keeping a desired distance to the net. The combined navigation and control system thus promotes safe and complete inspections of net pens, which are flexible 3D structures whose shape and position change and cannot be predetermined. In future work, we aim to further validate the method in the presence of fish, develop coverage planning methods, and further explore the method's potential as an experimental tool for analyzing the response of flexible underwater structures to environmental loads.

Acknowledgement

This work was supported by the Research Council of Norway (RCN) under the CHANGE project (grant no. 313737). The authors are grateful for the assistance sof SINTEF ACE during the sea trials.

REFERENCES

[1] FAO, *The State of World Fisheries and Aquaculture 2022. Blue Transformation in action*. Food and Agriculture Organization of the United Nations, 2024.

[2] O. M. Faltinsen and Y. Shen, "Wave and current effects on floating fish farms," *J. Marine Science and Applications*, vol. 17, pp. 284–296, 2018.

[3] B. Morro, K. Davidson, T. P. Adams, L. Falconer, M. Holloway, A. Dale, D. Aleynik, P. R. Thies, F. Khalid, J. Hardwick, H. Smith, P. A. Gillibrand, and S. Rey-Planellas, "Offshore aquaculture of finfish: Big expectations at sea," *Rev. Aquaculture*, vol. 14, no. 2, pp. 791–815, 2021.

[4] H. V. Bjelland, O. Folkedal, H. Moe Føre, E. I. Grøtli, I. M. Holmen, E. Lona, H. Slette, K. Størkersen, and T. Thorvaldsen, "Exposed aquaculture operations: Strategies for safety and fish welfare," *Reviews in Aquaculture*, vol. 0, pp. 1–13, 2024.

[5] H. Moe Føre, A. Fredheim, and O. S. Hopperstad, "Structural analysis of aquaculture net cages in current," *Journal of Fluids and Structures*, vol. 26, pp. 503–516, 2010.

[6] J. L. Saraiva, P. Rachinas-Lopes, and P. Arechavala-Lopez, "Finding the "golden stocking density": a balance between fish welfare and farmers' perspectives," *Frontiers in Veterinary Science*, vol. 9, p. 930221, 2022.

[7] R. Naylor, M. Troell, D. Little, R. Hardy, S. Bush, S. Shumway, J. Lubchenco, L. Cao, D. Klinger, and A. Buschmann, "A 20-year retrospective review of global aquaculture," *Nature*, vol. 591, p. 551, 03 2021.

[8] Ø. Jensen, T. Dempster, E. Thorstad, I. Uglem, and A. Fredheim, "Escapes of fish from Norwegian sea-cage aquaculture: causes, consequences, and prevention," *Aquaculture Environment Interactions*, vol. 1, pp. 71–83, Aug. 2010.

[9] H. Moe Føre and T. Thorvaldsen, "Causal analysis of escape of Atlantic salmon and rainbow trout from Norwegian fish farms during 2010–2018," *Aquaculture*, vol. 532, p. 736002, 2021.

[10] J. Bannister, M. Sievers, F. Bush, and N. Bloecher, "Biofouling in marine aquaculture: a review of recent research and developments," *Biofouling*, vol. 35, pp. 631–648, 2019.

[11] E. Kelasidi and E. Svendsen, "Robotics for sea-based fish farming," in *Encyclopedia of Smart Agriculture Technologies*, Q. Zhang, Ed. Cham: Springer International Publishing, 2022, pp. 1–20.

[12] P. Lader, D. Kristiansen, M. Alver, H. V. Bjelland, and D. Myrhaug, "Classification of aquaculture locations in Norway with respect to wind wave exposure," in *Proc. ASME 36th International Conference on Ocean, Offshore and Arctic Engineering*, vol. 6: Ocean Space Utilization, Jun. 2017.

[13] L. C. Gansel, S. Rackebrandt, F. Oppedal, and T. A. McClimans, "Flow fields inside stocked fish cages and the near environment," *Journal of Offshore Mechanics and Arctic Engineering*, vol. 136, Aug. 2014.

[14] F. A. Michelsen, P. Klebert, O. J. Broch, and M. O. Alver, "Impacts of fish farm structures with biomass on water currents: A case study from Frøya," *Journal of Sea Research*, vol. 154, p. 101806, 2019.

[15] P. Klebert and B. Su, "Turbulence and flow field alterations inside a fish sea cage and its wake," *Applied Ocean Research*, vol. 98, p. 102113, 2020.

[16] P. Rundtop and K. Frank, "Experimental evaluation of hydroacoustic instruments for ROV navigation along aquaculture net pens," *Aquaculture Engineering*, vol. 74, pp. 143–156, Sep. 2016.

[17] C. Schellewald, A. Stahl, and E. Kelasidi, "Vision-based pose estimation for autonomous operations in aquacultural fish farms," *IFAC-PapersOnLine*, vol. 54, no. 16, pp. 438–443, 2021, 13th IFAC Conference on Control Applications in Marine Systems, Robotics, and Vehicles (CAMS).

[18] O. M. Faltinsen, *Sea Loads on Ships and Offshore Structures*, ser. Cambridge Ocean Technology. Cambridge University Press, 1990.

[19] Y.-C. Li, Y.-P. Zhao, F.-K. Gui, and B. Teng, "Numerical simulation of the hydrodynamic behaviour of submerged plane nets in current," *Ocean Engineering*, vol. 33, no. 17, pp. 2352–2368, 2006.

[20] L. Li, S. Fu, and Y. Xu, "Nonlinear hydroelastic analysis of an aquaculture fish cage in irregular waves," *Marine Structures*, vol. 34, pp. 56–73, 2013.

[21] G. Løland, "Current forces on and flow through fish farms," Ph.D. dissertation, Department of Marine Technology, Norwegian University of Science and Technology, 1991.

[22] P. F. Lader and A. Fredheim, "Dynamic properties of a flexible net sheet in waves and current — a numerical approach," *Aquacultural Engineering*, vol. 35, no. 3, pp. 228–238, 2006.

[23] T. Kristiansen and O. M. Faltinsen, "Modelling of current loads on aquaculture net cages," *Journal of Fluids and Structures*, vol. 34, pp. 218–235, 2012.

[24] B. Su, E. Kelasidi, K. Frank, J. Haugen, M. Føre, and M. O. Pedersen, "An integrated approach for monitoring structural deformation of aquaculture net cages," *Ocean Engineering*, vol. 219, p. 108424, 2021.

[25] D. Marichal, "Cod-end numerical study," in *Proc 3rd International Conference on Hydroelasticity in Marine Technology*, 2003.

[26] V. Johansen, "Modelling of flexible slender systems for real-time simulation and control applications," Ph.D. dissertation, Department of Marine Technology, Norwegian University of Science and Technology, 2007.

[27] E. Katsidoniotaki, B. Su, E. Kelasidi, and T. Sapsis, "Integrating Machine Learning for Real-Time Structural Monitoring of Net Cages," in *International Ocean and Polar Engineering Conference*, 2024, pp. ISOPE–I–24–020.

[28] E. Katsidoniotaki, B. Su, E. Kelasidi, and T. P. Sapsis, "Multifidelity digital twin for real-time monitoring of structural dynamics in aquaculture net cages," 2024. [Online]. Available: https://arxiv.org/abs/2406.04519

[29] P. Lader, T. Dempster, A. Fredheim, and Ø. Jensen, "Current induced net deformations in full-scale sea-cages for atlantic salmon (salmo salar)," *Aquacultural Engineering*, vol. 38, no. 1, pp. 52–65, 2008.

[30] P. Klebert, Øystein Patursson, P. C. Endresen, P. Rundtop, J. Birkevold, and H. W. Rasmussen, "Three-dimensional deformation of a large

circular flexible sea cage in high currents: Field experiment and modeling," *Ocean Engineering*, vol. 104, pp. 511 – 520, 2015.

[31] J. DeCew, D. Fredriksson, P. Lader, M. Chambers, W. Howell, M. Osienki, B. Celikkol, K. Frank, and E. Høy, "Field measurements of cage deformation using acoustic sensors," *Aquacultural Engineering*, vol. 57, pp. 114–125, 2013.

[32] H. B. Amundsen, M. Xanthidis, M. Føre, S. J. Ohrem, and E. Kelasidi, "Aquaculture field robotics: Applications, lessons learned and future prospects," 2024. [Online]. Available: https://arxiv.org/abs/2404.12995

[33] A. Cardaillac, H. B. Amundsen, E. Kelasidi, and M. Ludvigsen, "Application of maneuvering based control for autonomous inspection of aquaculture net pens," in *8th Asia-Pacific Conference on Intelligent Robot Systems (ACIRS)*, 2023, pp. 44–51.

[34] H. B. Amundsen, W. Caharija, and K. Y. Pettersen, "Autonomous ROV inspections of aquaculture net pens using DVL," *IEEE J. Oceanic Eng.*, vol. 47, pp. 1–19, 2022.

[35] G. Livanos, M. Zervakis, V. Chalkiadakis, K. Moirogiorgou, G. Giakos, and N. Papandroulakis, "Intelligent navigation and control of a prototype autonomous underwater vehicle for automated inspection of aquaculture net pen cages," in *Proc. IEEE International Conference on Imaging Systems and Techniques (IST)*, Oct 2018.

[36] M. Bjerkeng, E. I. Grøtli, T. Kirkhus, J. T. Thielemann, H. B. Amundsen, B. Su, and S. Ohrem, "Absolute localization of an ROV in a fish pen using laser triangulation," in *2023 31st Mediterranean Conference on Control and Automation (MED)*, 2023, pp. 182–188.

[37] A. Duda, J. Schwendner, A. Stahl, and P. Rundtop, "Visual pose estimation for autonomous inspection of fish pens," in *OCEANS 2015 - Genova*, 2015, pp. 1–6.

[38] W. Akram, A. Casavola, N. Kapetanović, and N. Miškovic, "A visual servoing scheme for autonomous aquaculture net pens inspection using ROV," *Sensors*, vol. 22, no. 9, 2022.

[39] D. Botta, L. Ebner, A. Studer, V. Reijgwart, R. Siegwart, and E. Kelasidi, "Framework for robust localization of UUVs and mapping of net pens," 2024. [Online]. Available: https://arxiv.org/abs/2409.15475

[40] E. Kelasidi, B. Su, W. Caharija, M. Føre, M. Pedersen, and K. Frank, "Autonomous monitoring and inspection operations with UUVs in fish farms," *IFAC-PapersOnLine*, vol. 55, no. 31, pp. 401–408, 2022.

[41] D. Rosa, D. Cabecinhas, and F. Ferreira, "Forward-looking sonar based autonomous aquaculture inspection," in *OCEANS 2024 - Singapore*, 2024, pp. 1–8.

[42] H. B. Amundsen, M. Føre, S. J. Ohrem, B. O. A. Haugaløkken, and E. Kelasidi, "Three-dimensional obstacle avoidance and path planning for unmanned underwater vehicles using elastic bands," *IEEE Transactions on Field Robotics*, vol. 1, pp. 70–92, 2024.

[43] S. Quinlan and O. Khatib, "Elastic bands: connecting path planning and control," in *Proc. IEEE International Conference on Robotics and Automation*, 1993, pp. 802–807.

[44] M. Xanthidis, M. Skaldebø, B. Haugaløkken, L. Evjemo, K. Alexis, and E. Kelasidi, "ResiVis: A holistic underwater motion planning approach for robust active perception under uncertainties," *IEEE Robotics and Automation Letters*, vol. 9, no. 11, pp. 9391–9398, 2024.

[45] T. I. Fossen, *Handbook of Marine Craft Hydrodynamics and Motion Control*. John Wiley & Sons Ltd., 2021.

[46] R. Courant, K. Friedrichs, and H. Lewy, "On the partial difference equations of mathematical physics," *IBM Journal of Research and Development*, vol. 11, no. 2, pp. 215–234, 1967.

[47] T. Kristiansen and O. M. Faltinsen, "Experimental and numerical study of an aquaculture net cage with floater in waves and current," *Journal of Fluids and Structures*, vol. 54, pp. 1–26, 2015.

[48] M. Skaldebø, S. J. Ohrem, H. B. Amundsen, E. Kelasidi, and N. Bloecher, "Framework for autonomous navigation for a permanent resident aquaculture net grooming robot," in *31st Mediterranean Conference on Control and Automation (MED)*, 2023, pp. 356–363.

[49] K.-J. Reite, M. Føre, K. G. Aarsæther, J. Jensen, P. Rundtop, L. T. Kyllingstad, P. C. Endresen, D. Kristiansen, V. Johansen, and A. Fredheim, "FhSim - time domain simulations of marine systems," in *Proc. ASME 33rd International Conference on Ocean, Offshore and Arctic Engineering*, 2014.

[50] E. Børhaug, L. Pivano, K. Y. Pettersen, and T. A. Johansen, "A model-based ocean current observer for 6DOF underwater vehicles," *IFAC Proceedings Volumes*, vol. 40, no. 17, pp. 169–174, 2007, 7th IFAC Conference on Control Applications in Marine Systems.

[51] M. Breivik and T. Fossen, "Principles of guidance-based path following in 2D and 3D," in *Proc. 44th IEEE Conference on Decision and Control*, 2005, pp. 627–634.

[52] I. Castillo, L. Fridman, and J. A. Moreno, "Super-twisting algorithm in presence of time and state dependent perturbations," *International Journal of Control*, vol. 91, no. 11, pp. 2535–2548, 2018.

[53] B. O. A. Haugaløkken, H. B. Amundsen, H. S. Fadum, J. T. Gravdahl, and S. J. Ohrem, "Adaptive generalized super-twisting tracking control of an underwater vehicle," in *Proc. IEEE Conference on Control Technology and Applications (CCTA)*, 2023, pp. 687–693.

[54] SINTEF, "ACE," https://www.sintef.no/en/all-laboratories/ace/, 2023, accessed: 2023-04-25.

[55] L. C. Gansel, D. R. Plew, P. C. Endresen, A. I. Olsen, E. Misimi, J. Guenther, and Ø. Jensen, "Drag of clean and fouled net panels – measurements and parameterization of fouling," *PLOS ONE*, vol. 10, no. 7, pp. 1–17, 07 2015.

[56] M. Bloesch, S. Omari, M. Hutter, and R. Siegwart, "Robust visual inertial odometry using a direct EKF-based approach," in *IEEE/RSJ International Conference on Intelligent Robots and Systems (IROS)*, 2015, pp. 298–304.

[57] E. Galceran, R. Campos, N. Palomeras, D. Ribas, M. Carreras, and P. Ridao, "Coverage path planning with real-time replanning and surface reconstruction for inspection of three-dimensional underwater structures using autonomous underwater vehicles," *Journal of Field Robotics*, vol. 32, no. 7, pp. 952–983, 2015.

[58] S. M. Holen, I. B. Utne, I. M. Holmen, and H. Aasjord, "Occupational safety in aquaculture – part 2: Fatalities in Norway 1982–2015," *Marine Policy*, vol. 96, pp. 193–199, 2018.

[59] S. Espelid, G. B. Løkken, K. Steiro, and J. Bøgwald, "Effects of cortisol and stress on the immune system in Atlantic Salmon (Salmo salar L.)," *Fish & Shellfish Immunology*, vol. 6, no. 2, pp. 95–110, 1996.

[60] M. Kruusmaa, R. Gkliva, J. Tuhtan, A. Tuvikene, and J. A. Alfredsen, "Salmon behavioural response to robots in an aquaculture sea cage," *Royal Society open science*, vol. 7, no. 3, p. 191220, 2020.

[61] Q. Zhang, N. Bloecher, L. D. Evjemo, M. Føre, B. Su, E. Eilertsen, M. A. Mulelid, and E. Kelasidi, "Farmed Atlantic salmon (Salmo salar L.) avoid intrusive objects in cages: The influence of object shape, size and colour, and fish length," *Aquaculture*, vol. 581, p. 740429, 2024.

HERMAN B. AMUNDSEN (Member, IEEE) received the M.Sc. degree in cybernetics and robotics from the Norwegian University of Science and Technology (NTNU), Trondheim, Norway, in 2020.

Since 2020, he has been with SINTEF Ocean, Trondheim, Norway, where he has been researching robotics and automation in aquaculture. In 2021, he started his Ph.D. education at the Dept. of Engineering Cybernetics at NTNU. His Ph.D. research subject is on the development of autonomous control strategies for unmanned underwater vehicles operating in dynamically changing environments such as fish farms, and he has published more than 15 peer-reviewed papers.

Mr. Amundsen is a member of the Norwegian Society of Graduate Technical and Scientific Professionals (Tekna). He has been a reviewer for IEEE Transactions on Systems, Man, and Cybernetics: Systems, IEEE Transactions on Control System Technology, IEEE Transactions on Automation Science and Engineering, IEEE Transactions on Robotics, IEEE Robotics and Automation Letters, and IEEE/CAA Journal of Automatica Sinica.

EIRINI KATSIDONIOTAKI received a Ph.D. degree in computational engineering from Uppsala University, Sweden, where she focused on the resilience of offshore structures for renewable energy under extreme wave conditions. She also holds an M.Sc. in energy production and management from the National Technical University of Athens, Greece, and a Diploma in mechanical and aeronautic engineering from the University of Patras, Greece.

Since 2023, she has been a Postdoctoral Fellow at the Department of Mechanical Engineering at the Massachusetts Institute of Technology (MIT), USA. Her research leverages machine learning and statistical methods to develop predictive models for ocean structures, including net pens for aquaculture, and frameworks to forecast extreme events in complex dynamical systems. During her Ph.D., she utilized computational fluid dynamics (CFD) to model wave energy devices and developed reduced-order models that effectively predict extreme loads, reducing computational costs.

Dr. Katsidoniotaki is a recipient of a prestigious Wallenberg Foundation postdoctoral fellowship and serves as a reviewer for journals such as Ocean Engineering and Applied Ocean Research. She is also a member of the Society of Industrial and Applied Mathematics (SIAM).

MARTIN FØRE is an Associate Professor at the Department of Engineering Cybernetics at the Norwegian University of Science and Technology (NTNU) in Trondheim, the same department at which he received his M.Sc. (2006) and Ph.D. (2011) degrees within engineering cybernetics.

Before he started his current job as an Associate Professor at NTNU in 2019, he worked as a Research Scientist/Senior Research Scientist at SINTEF Fisheries and Aquaculture/SINTEF Ocean in Trondheim from 2011-2018. Previous to this, he worked as a part-time (25%) Research Fellow at SINTEF Fisheries and Aquaculture, while doing his Ph.D. at NTNU (2006-2011). His main field of research is the application of cybernetic methods within aquaculture, fisheries and marine biology. To date, he has published more than 60 peer-reviewed scientific articles, conference papers and book chapters within these areas.

Assoc.Prof. Føre is a member of the Norwegian Society of Graduate Technical and Scientific Professionals (Tekna), and is a Knight of the Golden Feedback Loop at NTNU.

ELENI KELASIDI (Member, IEEE), is a Senior Research Scientist and head of SINTEF ACE-RoboticLab - Autonomous and Robotic Aquaculture systems Lab in SINTEF Ocean leading activities on autonomous systems and robotic solutions applied to the aquaculture industry and targeting interdisciplinary research to link the field of technology and biology. Eleni Kelasidi received the Diploma (MSc) of electrical and computer engineering and the Ph.D degree in engineering cybernetics from the University of Patras in 2009 and from Norwegian University of Science and Technology (NTNU), Trondheim in 2015, respectively. In 2009-2012, she was a pre-doc researcher in the field of design and control of mobile robot with articulated body at the University of Patras. In 2016, she was honored three-year VISTA (as a collaborative partnership between Statoil and the Norwegian Academy of Science and Letters) fellowship investigating resident robot manipulators for subsea IMR operations as a PostDoc Researcher (VISTA Scholar) at the CoE Centre for Autonomous Marine Operations and Systems, NTNU.

In 2020, she was granted the Young Researcher Talent funding from Research Council of Norway to perform research on unmanned underwater vehicles operating in dynamically changing environments. She has acquired several projects targeting both fundamental knowledge and applied research and investigated problems towards the realization of autonomous robotic concepts in the aquaculture domain. Her research group's work on robotic applications in the fish farming industry led to the development of the first robotic lab dedicated to the aquaculture domain. In period 2023-2024, she had been in research visit at Sea Grant, MIT and at the Autonomous Systems Lab (ASL), ETH. She has received several awards including the SINTEF's outstanding research award in 2024 for developing robotics and autonomy in aquaculture as a new research area. Her main research areas are automation and robotics dedicated for aquaculture, biology-technology interaction, underwater snake robots, dynamics modeling and nonlinear control and autonomous systems.